AD________________

Award Number: DAMD17-03-1-0558

TITLE: Development and Characterization of Novel Olumetric Acquisition Orbits with an Application Specific Emission Tomograph for Improved Breast Cancer Detection

PRINCIPAL INVESTIGATOR: Martin P. Tornai
Caryl N. Brzymialkiewicz

CONTRACTING ORGANIZATION: Duke University
Durham, North Carolina 27708-0491

REPORT DATE: August 2004

TYPE OF REPORT: Annual Summary

PREPARED FOR: U.S. Army Medical Research and Materiel Command
Fort Detrick, Maryland 21702-5012

DISTRIBUTION STATEMENT: Approved for Public Release;
Distribution Unlimited

20050218 112

REPORT DOCUMENTATION PAGE

Form Approved
OMB No. 074-0188

1. AGENCY USE ONLY (Leave blank)	**2. REPORT DATE** August 2004	**3. REPORT TYPE AND DATES COVERED** Annual Summary (14 Jul 2003 - 13 Jul 2004)

4. TITLE AND SUBTITLE
Development and Characterization of Novel Olumetric Acquisition Orbits with an Application Specific Emission Tomograph for Improved Breast Cancer Detection

5. FUNDING NUMBERS
DAMD17-03-1-0558

6. AUTHOR(S)
Martin P. Tornai
Caryl N. Brzymialkiewicz

7. PERFORMING ORGANIZATION NAME(S) AND ADDRESS(ES)
Duke University
Durham, North Carolina 27708-0491

E-Mail: Cnb3@duke.edu

8. PERFORMING ORGANIZATION REPORT NUMBER

9. SPONSORING / MONITORING AGENCY NAME(S) AND ADDRESS(ES)
U.S. Army Medical Research and Materiel Command
Fort Detrick, Maryland 21702-5012

10. SPONSORING / MONITORING AGENCY REPORT NUMBER

11. SUPPLEMENTARY NOTES

12a. DISTRIBUTION / AVAILABILITY STATEMENT
Approved for Public Release; Distribution Unlimited

12b. DISTRIBUTION CODE

13. ABSTRACT (Maximum 200 Words)

Nuclear medicine based molecular imaging techniques can be used as an adjunct tool in the diagnosis of breast cancer, particularly for women with dense breast tissue. The dedicated emission mammotomograph is now fully functional; the tomographic gantry was enhanced by including an automated radius-of-rotation capability, to allow for fully 3D imaging of a pendant, uncompressed breast. As a result, novel 3D acquisition orbits have been developed to contour various sized breasts. Initial phantom measurements with a 16x20cm^2 field-of-view cadmium zinc telluride detector show the capability of the system to acquire data about concentric hemispheres of the breast, minimizing distance-dependent spatial resolution effects, maximizing the viewable breast volume while more-nearly-completely sampling the breast, and minimizing background contamination from the heart and liver. Results indicate 3D mammotomography, incorporating a compact CZT detector and unique 3D camera trajectories, is a promising dedicated breast imaging technique for visualization of tumors less than 1cm in diameter. Future work includes evaluation of: patient bed shielding, sampling schemes for various shaped breasts, and axillary imaging.

14. SUBJECT TERMS
Nuclear Medicine Imaging, SPECT, Dedicated Tomographic Breast Imaging

15. NUMBER OF PAGES
44

16. PRICE CODE

17. SECURITY CLASSIFICATION OF REPORT Unclassified	**18. SECURITY CLASSIFICATION OF THIS PAGE** Unclassified	**19. SECURITY CLASSIFICATION OF ABSTRACT** Unclassified	**20. LIMITATION OF ABSTRACT** Unlimited

NSN 7540-01-280-5500

Standard Form 298 (Rev. 2-89)
Prescribed by ANSI Std. Z39-18
298-102

Table of Contents

Introduction

Breast cancer is the second leading cause of cancer death in women, behind lung cancer alone. However, death rates have been declining, it is believed due to earlier detection and improved treatment; a patient's chances of survival dramatically increase if the breast cancer is small at the time it is diagnosed. The size and spread of the cancer are key factors in the patient's prognosis. With the early detection of a primary breast cancer, treatments are typically more effective given that there is less chance of metastasis. Furthermore, treatment of a small tumor allows for more limited surgery with breast conservation and significantly reduces morbidity and mortality. One goal, then, is to develop techniques which allow for earlier detection of a primary breast cancer. The overall objective of this work is to develop, implement and evaluate a novel, compact, dedicated emission mammotomography molecular imaging system. By developing and investigating a system capable of positioning the detector anywhere within a hemispherical volume about a pendant, uncompressed breast, we hope to improve detection (identification) and potentially characterization of breast cancer. Innovative, fully three-dimensional, volumetric data acquisition orbits, not previously possible with clinical scanners, will be developed and investigated.

Body

Task 1(a). The first key task was to implement and characterize a modified basis set of orbits, after implementing a dynamic radius-of-rotation (ROR) control. In the first prototype emission mammotomography system, the gantry incorporated two laboratory jacks, a goniometric cradle, and a rotation stage (models BGM200PE goniometer, RV350CC rotation stage, and M-EL80 jacks, *Newport Corp.,* Irvine, CA), providing for a manually-controlled radius-of-rotation (ROR), variations in polar angle, and rotational azimuthal motions, respectively. To connect the stages, custom-made aluminum plates were designed and built. Combined, the three degrees of motion permitted contiguous orbits on inverted hemispherical volumes [1, 2]. The camera can move in an absolute range of 0° to 90° polar (tilt) angles and a full 0° through 360° azimuthal angles, and a range of radii. At this stage of system development, in order to contour an object, the ROR, defined as the perpendicular distance between the detector face and the center-of-rotation (COR), was manually controlled (Fig. 1 (a), (b)). Subsequent implementation of a stepping motor (Model L511BTG2-012EL6, *Sanyo Denki*, Torrance, CA) provided for the automation and control of the ROR parameter (Fig. 1 (c)-(f)). The motor was attached to the cradle at one end and connected to the lab jacks with a timing belt, to raise and lower the camera, thus decreasing and increasing the ROR (Fig. 2), respectively. In order to control the motor, the power to the motor, the tachogenerator, and the optical encoder were appropriately connected to the motion control processor (model ESP-7000, *Newport Corp.*). As a result of the automated ROR, at all points of each step-and-shoot orbit acquisition, the software can position the camera as close to the phantom as possible.

Studies performed with the ASET using a high performance compact and quantized scintillator-based (NaI(Tl)) gamma camera have demonstrated its ability to achieve substantially decreased ROR as compared to the clinical gamma camera [1-3]. With an upgrade to a larger field-of-view (FOV), heavier semiconductor-based (cadmium-zinc-telluride (CZT)) camera, several modifications to the gantry were required. The dual-lab-jack ROR capability was replaced by a single, larger jack (model M-EL120, *Newport Corp.*) (Fig. 1(f)). Although using a substantially thinner CZT camera, the somewhat thicker jack meant the ROR range was actually about the same as that of the dual-jack, NaI(Tl) combination (range: 9.7 cm for CZT+gantry, 9.4 cm for NaI(Tl)+gantry). Additionally, software upgrades also accompanied the CZT camera, particularly because two computers are currently required to acquire and process the data. Thus, we had to modify the software to completely control the gantry and again synchronize acquisition and motion. The current system, with completely synchronized data acquisition and gantry movement, employing a dynamic ROR capability, is shown in Fig. 3.

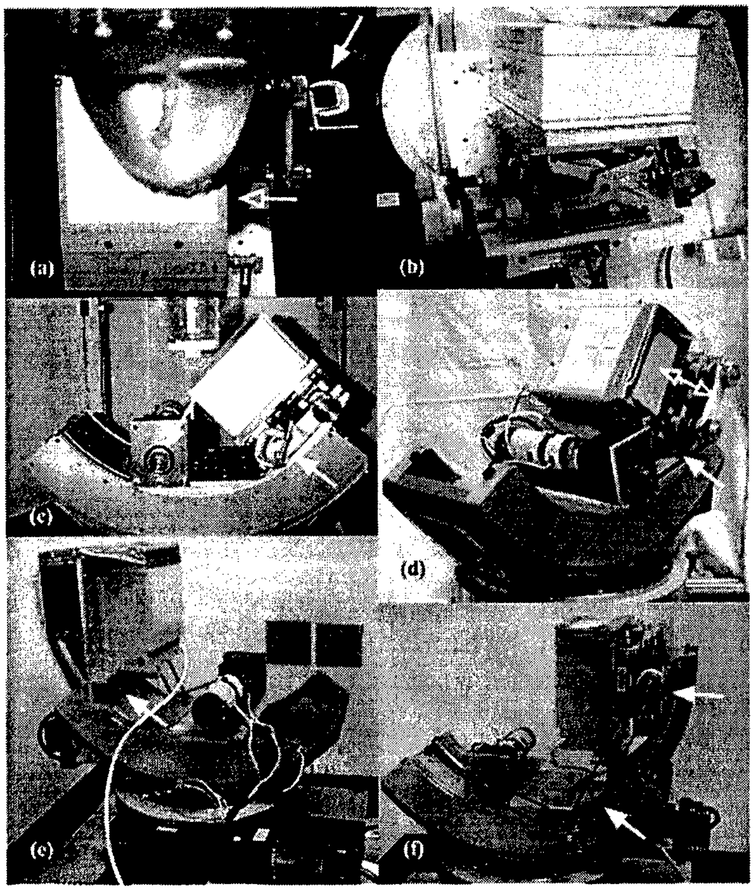

Figure 1: Photographs of various stages of ROR development. (a) Shifted gamma camera (open arrow head, to increase the FOV of the smaller detector) and manual ROR contouring control (small C-clamp, solid white arrow); (b) side view of shifted gamma camera; (c) Motor attached to goniometer; at this stage, manual ROR control; (d) Addition of single timing belt to dual M-EL80 jacks; complete automated ROR control; (e) Preparation for the arrival of the larger dimension CZT; plate designed to securely fasten both NaI-based and CZT-based cameras to the goniometric cradle; (f) Due to weight of the CZT camera, the single M-EL120 jack was implemented. A new timing belt mechanism allows for full range of CZT camera motion. In this photo, the 'combination' adapter plate is utilized with the NaI-based camera.

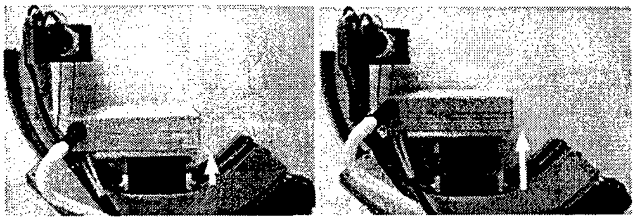

Figure 2: Photographs of (LEFT) larger ROR; (RIGHT) smaller ROR.

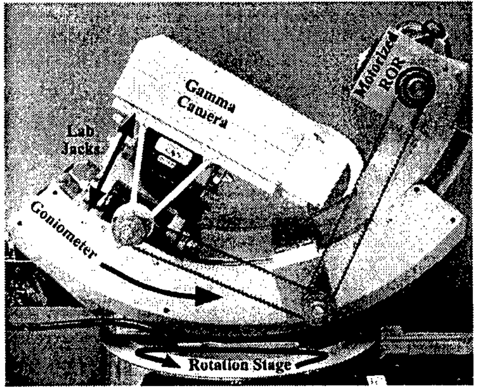

Figure 3: The current dedicated emission mammotomography system. The lab jack(s) provide for changes in the radius-of-rotation (ROR); the goniometer allows polar (ϕ) camera tilt; and the rotation stage provides for azimuthal variations (θ).

Task 1(b). Because the ASET is meant as a diagnostic device, the suspected lesion location may be known prior to the scan, in which case it may be advantageous to position the arc of CPA in the suspected quadrant, thus allowing for extended proximity to that portion of the breast (for example, Fig. 4). The arc can conform to the shape of the breast by dynamically changing the ROR, minimizing resolution degradation. While breast cancer most often occurs in the upper outer breast quadrant, suggesting perhaps that CPA with a θ=45° arc location may be optimal for imaging lesions in that particular quadrant (see Fig. 5 for azimuthal positioning orientation relative to the torso schematic), the entire breast should be imaged, necessitating an orbit modification which provides for uniform resolution characteristics throughout breast quadrants.

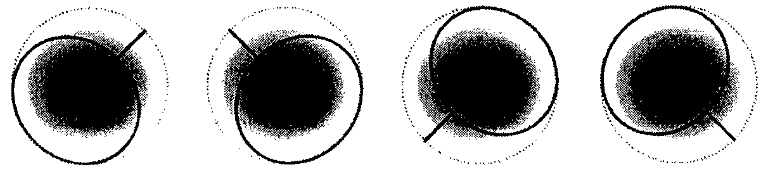

(a) $\theta=45^\circ$ (b) $\theta=135^\circ$ (c) $\theta=225^\circ$ (d) $\theta=315^\circ$

Figure 4: Anterior-posterior view of CPA with different azimuthal start locations relative to the pendant, uncompressed breast (centered, grey ellipse). Dashed circle defines equatorial diameter of the hemisphere.

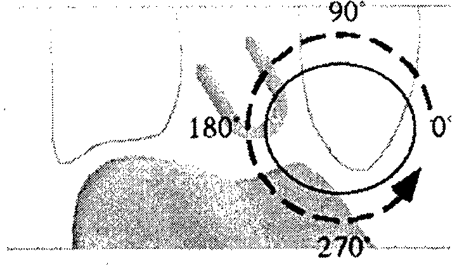

Figure 5: Schematic diagram of the frontal view of the anthropomorphic phantom, with approximate locations of the myocardium, liver and lungs in gray, and breast in black.

The Cloverleaf orbit is generated by taking the circular portion of the CPA only, rotating and superimposing into each quadrant (Fig. 6). But, because these overlapping circles result in the regions near the nipple becoming too densely sampled, the trajectory following the envelope about each circle that does not intersect the remaining three is used in the cloverleaf orbit. Cloverleaf is created by establishing a relationship between dθ and dϕ, such that the maximum amplitude (and thus maximum camera polar tilt) and spacing between projections can be easily modified. The number of 'leafs' can also be easily modified. An inverse Mercator projection is used to project the given functions onto the hemisphere: $\phi=gd(y)$ and $\theta=x+\theta_o$, where in this case, $\theta=0^o$ and gd is the Gudermannian Function [4], defined by: $gd(y) = 2\tan^{-1}(e^x)-0.5\pi$.

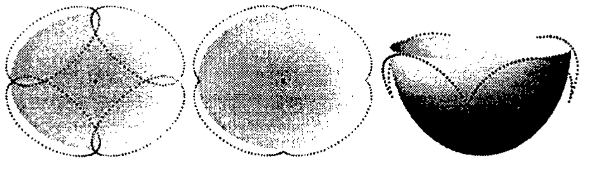

(a) (b) (c)

Figure 6: (a) Coronal schematic of multiple overlapping circles of CPA. Central nipple region is densely sampled. (b) Coronal schematic of envelope of the orbits at (a), otherwise seen as a 'cloverleaf'. (c) 3D perspective of cloverleaf with super-imposed breast hemi-ellipsoid.

As shown in Appendix B, the motivation behind the creation of 'InvCloverleaf', the 'inverse' cloverleaf, was to utilize the arc portion of CPA, rotating and superimposing, rather than the circle, then allowing for a smooth transition between quadrants. At its extreme, the inverse cloverleaf orbit could simply be two orthogonal linear trajectories (an "X") crossing at the nipple; such an orbit has been proposed for a pinhole collimated gamma camera [5].

Once the parameters of ϕ and θ are established from the orbit creation, it is then desirable to contour the breast and thus calculate the ROR. By modeling the breast shape as a hemi-ellipsoid, or a set of hemi-ellipsoids with different major axis lengths, and estimating the COR offset into the breast, the ROR can be determined based on an intersection of the camera position and the modeled breast.

Task 1(c). Phantom measurements using the modified orbits were performed; results from this work were presented at the 2004 *International Workshop on Digital Mammography*, 18-22 June, Durham, NC. A manuscript was subsequently submitted, to be published in its peer-reviewed conference record. Please see the attached article, C.N. Archer, *et al.*,"Evaluation of 3D Acquisition Orbits with an Emission Mammotomography System incorporating a full-field CZT Detector", Appendix B, for detailed descriptions of the work and results.

Task 2(a). For each orbit, an Orlov Volume can be calculated and consists of the set of voxels such that if and only if all activity is contained within those voxels, then by Orlov's condition, the orbit of the utilized parallel-beam collimator provides complete information from which to reconstruct activity on the support corresponding to those voxels [6]. (Finite gantry-angle stepsize, finite detector-bin width, camera spatial resolution, scatter, and Poisson noise limit the resolution to which activity within the Orlov Volume can be reconstructed.) For untilted vertical-axis-of-rotation (VAOR) orbits (tilted-parallel-beam (TPB) with tilt = 0°), the Orlov Volume is a cylinder. For orbits involving camera tilt, previous calculations have shown that the Orlov Volume for Circle-plus-two-arcs (CP2A) is indeed non-zero [6], yielding little to no artifacts in simulation [7]. Calculations of the shapes and volumes of Orlov Volumes for a sample set of trajectories are shown in Fig. 7, with a display threshold of 95%; this threshold is the percent solid angle (0-100) that is sampled. Even in the case of VAOR, 100% was not achieved, presumably due to discretization and binning effects. VAOR provides for the maximal achievable volume, determined by the program as 5427 cm^3. The volume of a cylinder is $\pi R2h$, where R is the radius and h is the height. Given our geometry and detector (h=16 cm and R=10 cm) we would expect a volume of 5026 cm^3. The overestimation by 8% may be due to binning effects, similar to that seen in [6].

While this work focuses on parallel-beam imaging, utilizing a focal spot at infinity, Orlov's sampling criteria have been shown to be a special case [6,8] of Tuy's condition for cone-beam sampling [9], which outlines criteria for cone-beam type collimation geometries that are easily adaptable to our system. The flexibility of the gantry allows for investigation of an infinite number of sampling schemes, for a variety of converging or even diverging collimation beam configurations and camera sizes.

Some of the orbits presented in Fig. 7 have been evaluated previously in [1,2], utilizing a smaller field-of-view (FOV) scintillator-based detector and 940ml breast phantom from *Data Spectrum Corp.* (Hillsborough, NC). Our lab has recently acquired an anthropomorphic torso phantom (*Radiology Support Devices*, Newport Beach, CA) and six custom anthropomorphic breast phantoms (Fig. 8). Orbits have been designed to optimally contour each. Preliminary results have been submitted and accepted to the *IEEE Nuclear Science Symposium and Medical Imaging Conference,* which will be held in Rome, Italy, 16-22 October 2004. Please see Appendix C for the preliminary measurements associated with Task 2(a).

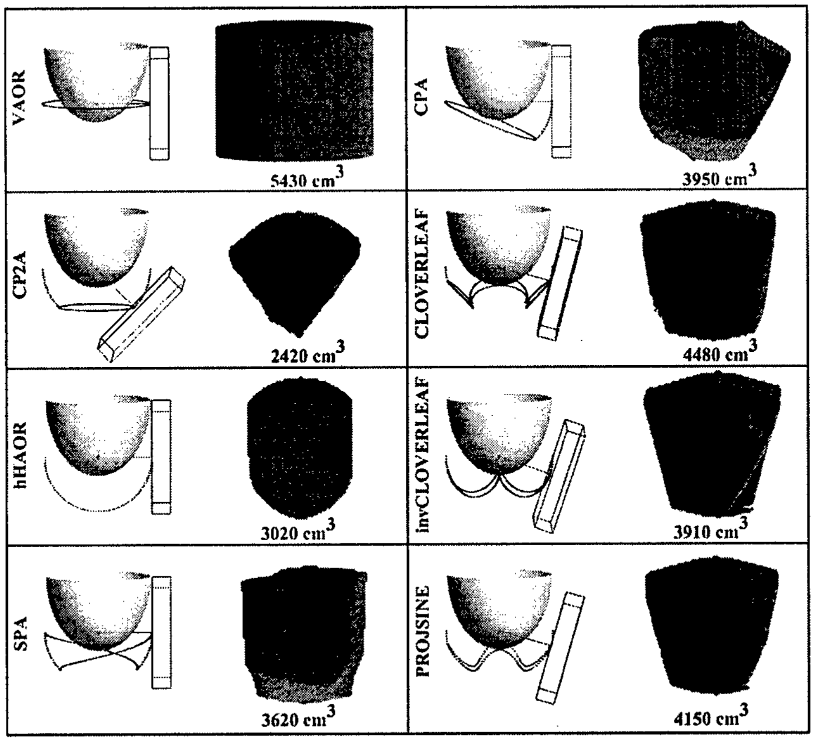

Figure 7: Within each box, the LEFT schematic is a scale schematic of the orbit, with an isolated 1060ml breast modeled. The orbits are Vertical-Axis-of-Rotation (VAOR); Circle-Plus-Arc (CPA); Circle-Plus-Two-Arcs (CP2A); Cloverleaf; half-Horizontal-Axis-of-Rotation (hHAOR); Inverse Cloverleaf (invCloverleaf); Spiral-Plus-Arcs (SPA); and Sine Projection (PROJSINE). The wire-frame box represents the detector (here, the 16x20 cm^2 active detector field-of-view of the CZT camera), with camera center on the trajectory (black orbit path) about the breast. Orbits are illustrated here with equal and fixed ROR of 8.5 cm for ease of illustration. The dark gray line from the COR is perpendicular to the detector face. The RIGHT schematic in each box is the Voxelized Orlov Volume for each orbit, in the pendant breast reference frame. Again, the camera FOV is 16x20 cm^2; each voxel is 0.25 cm on a side. Note that volume schematics are not to scale; volumes are given below each calculated shape.

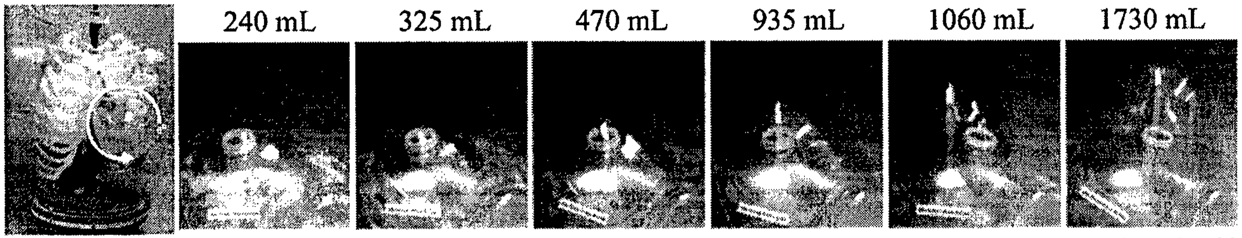

Figure 8: (FAR LEFT) Photograph of the upright positioned torso phantom (*Radiology Support Devices*, Newport Beach, CA), with labeled detector azimuth location relative to one pendant, uncompressed breast. Note also the (color and radioactivity) filled heart and liver. (RIGHT) Photographs of the six *Radiology Support Devices* breast phantoms with various volumes, as labeled.

Task 3(a), (b). Task 3 is closely related to the ongoing work of Task 2. Therefore, the timeline of the statement of work has been slightly modified in that Task 3 is ongoing concurrently with the other tasks. My advisor's NIH grant to develop Simultaneous Emission and Transmission Mammotomography allowed us to purchase a 16x20cm^2 field-of-view (FOV) cadmium-zinc-telluride (CZT) detector. Initial cold rod and cold disk phantom measurements were made for the new CZT detector. Because this camera has a larger FOV than our previous NaI(Tl)-based detector, and can provide for improved energy resolution, we were eager to evaluate orbits created from Task 2(a) with and without additional torso backgrounds for this new detector. Initial characterization of the camera resulted in my attendance at the *2003 IEEE Nuclear Science Symposium & Medical Imaging Conference*, 19-25 October, Portland, OR; subsequently, results were published in its conference record. Further orbit refinement and experimentation lead to a submission to *IEEE Transactions of Medical Imaging* (submitted July 15, 2004, see attached article for details, Appendix D). Additionally, my advisor and I felt it would be a unique opportunity to learn about various types of discrete imaging detectors by participating in a set of experiments to characterize and compare NaI-based cameras with different pixellation (different detector arrays), resulting in a submission to *IEEE Transactions of Nuclear Science*, currently in review (see Appendix E).

Key Accomplishments

Year 1 originally included tasks 1 and 2(a) from the Statement of Work (SOW) (included as Appendix A). Summarizing specific progress:

- Task 1 was completed in its entirety, including implementation of a motorized, dynamically controlled radius-of-rotation capability for the system. Several programs were written in Matlab^{TM} (The MathWorks, Inc., Natick, MA) to automate the orbit creation process for circle-plus-arc type orbits with various degrees of tilt and arc locations (the automation itself is also a part of task 2(d)). In addition, several other types of orbits, including: cloverleaf, inverse cloverleaf, and 'projsine' were implemented. Results from this work were presented at the 2004 *International Workshop on Digital Mammography*, 18-22 June, Durham, NC and a manuscript was submitted to be published in its conference record (see attached article, C.N. Archer, *et al.*,"Evaluation of 3D Acquisition Orbits with an Emission Mammotomography System incorporating a full-field CZT Detector", Appendix B.)

- Task 2(a) has also been completed, utilizing Matlab^{TM} scripts and calculations of Orlov Volumes for a variety of breast sizes and shapes. Our lab recently acquired an anthropomorphic torso phantom (*Radiology Support Devices Inc.*, Newport Beach, CA) and six custom anthropomorphic breast phantoms (volumes ranging from 240ml to 1730ml), in addition to one compressible breast phantom. The dimensions of each were modeled, and orbits were designed to optimally contour each. Preliminary results were submitted and accepted to the *IEEE Nuclear Science Symposium and Medical Imaging Conference*, to be held in Rome, Italy, October 2004 (see Appendix C). This work will be presented as a poster at the conference; an accompanying manuscript will be submitted to the conference record.

- Task 3 is ongoing concurrently with the other tasks. This is a slight deviation from the original timeline of the SOW. As a result of my advisor's NIH grant to develop Simultaneous Emission and Transmission Mammotomography, we were able to purchase a 16x20cm^2 field-of-view (FOV) cadmium-zinc-telluride (CZT) detector. Because this camera has a larger FOV than our previous NaI(Tl)-based detector, and can provide for improved energy resolution, we were eager to evaluate orbits created from Task 2(a) with and without additional torso backgrounds for this new detector. Initial characterization of the camera resulted in my attendance at the *2003 IEEE Nuclear Science Symposium & Medical Imaging Conference*, 19-25 October, Portland, OR; subsequently, results were published in its conference record. Further orbit refinement and experimentation lead to a submission to *IEEE Transactions of Medical Imaging* (submitted July 15, 2004, see attached article for details, Appendix D).

Related:

- In addition to the tasks listed in the SOW, I felt it would be a unique opportunity to learn about various types of discrete imaging detectors by participating in a set of experiments to characterize and compare various NaI-based cameras, resulting in a submission to *IEEE Transactions of Nuclear Science*, currently in review (see Appendix E).

- Because of the continued growth of our lab, this past year I have had the opportunity to work directly with my fellow graduate student, Randolph McKinley. Through this interaction, I have gained exposure to the transmission portion of the system, developing my skills in x-ray imaging, in addition to my chosen modality. Furthermore, our lab will grow by the addition of three students starting in September, providing further opportunity to mentor and educate.

- As mentioned in the grant, this work has formed the general outline for my dissertation thesis. As a direct result of this work, my dissertation committee was formed, and my thesis proposal was accepted September 16, 2004.

Reportable Outcomes

Peer-Reviewed

C.N. Brzymialkiewicz, R.L. McKinley, M.P. Tornai, "Evaluation of 3D Acquisition Orbits with an Emission Mammotomography System Incorporating a Full-Field CZT Detector", Presented at the *International Workshop on Digital Mammography*, 18-21 June 2004, Durham, NC, and submitted to *Proc. Of 7th International Workshop on Digital Mammography.*

C.N. Brzymialkiewicz, M.P. Tornai, R.L. McKinley, and J.E. Bowsher, "Evaluation of Fully 3D Emission Mammotomography with a Compact Cadmium Zinc Telluride Detector", Submitted to *IEEE Transactions on Medical Imaging,* July 2004.

M.P. Tornai, C.N. Brzymialkiewicz, M.L. Bradshaw, J.E. Bowsher, B.E. Patt, J.S. Iwanczyk, J. Li, L.R. MacDonald, "Comparison of Compact Gamma Cameras with 1.3mm and 2.0mm Quantized Elements for Dedicated Emission Mammotomography", *IEEE Transactions on Nuclear Science*, 2004, In Revision.

Conference Proceedings

C.N. Archer and M.P. Tornai, "Investigation of Full-Field CZT Detector for Emission Mammotomography," Presented at the *2003 IEEE Nuclear Science Symposium & Medical Imaging Conference*, Portland, OR 19-25 Oct. 2003, and published in *2003 IEEE Conference Record NSS/MIC,* CD-ROM ISBN 0-7803-8258-7 (paperbound forthcoming).

R.L. McKinley, E. Samei, C.N. Brzymialkiewicz, M.P. Tornai, C.E. Floyd, "Measurements of an Optimized Beam for X-ray Computed Mammotomography," *Proc. SPIE: Physics of Medical Imaging,* 5389:311-319, 2004.

Presentations

M.P. Tornai, C.N. Archer, J.E. Bowsher, "Non-invasive 3-dimensional molecular imaging of early breast cancer with a dedicated mammotomograph," Presented at the *26th Annual San Antonio Breast Cancer Symposium,* San Antonio, TX 3-6 Dec. 2003.

C.N. Brzymialkiewicz and M.P. Tornai, "Development and Evaluation of an Emission Mammotomography for Improved Breast Cancer Detection," Presented at Duke University, *4th Annual Graduate Student Research Day*, 24 March 2004.

C.N. Brzymialkiewicz, M.P. Tornai, R.L. McKinley, and J.E. Bowsher, "3D Data Acquisition Sampling Strategies for Dedicated Emission Mammotomography for Various Breast Sizes," To be presented at the 2004 IEEE NSS/MIC, October, Rome, Italy.

Funding

Received a NIH Student Travel Award in the amount of $500 to help defray costs to attend the 2004 IEEE NSS/MIC (to be held in October in Rome, Italy) and present results from my submitted and accepted abstract.

Conclusions

The dedicated emission mammotomography system, in its current implementation with a 16x20cm^2 FOV semiconductor-based (CZT) detector with 2.5mm^2 pixels has demonstrated the flexibility of the imaging system to image a pendant breast, including those of various shapes and sizes, using unique 3D camera trajectories. Results indicate 3D mammotomography using clinically relevant scan times and radiopharmaceutical doses is a promising dedicated breast imaging technique for visualization of tumors less than 1cm in diameter. For inconclusive mammographic studies, or for women with dense breasts, for example, this system could be used as a secondary diagnostic tool. Future work includes evaluation of patient bed shielding, sampling schemes for various shaped breasts, and axillary imaging.

References

[1] C.N. Archer, M.P. Tornai, J.E. Bowsher, S.D. Metzler, B.C. Pieper, and R.J. Jaszczak. Implementation and initial characterization of acquisition orbits with a dedicated emission mammotomograph. *IEEE Trans. Nucl. Sci.*, 50(3):418–420, 2003.

[2] M.P. Tornai, J.E. Bowsher, C.N. Archer, J. Peter, R.J. Jaszczak, L.R. MacDonald, B.E. Patt, and J.S. Iwanczyk. A 3d gantry single photon emission tomograph with hemispherical coverage for dedicated breast imaging. *Nucl. Inst. & Meth. Phys. Res. A*, A497(1):157–167, 2003.

[3] B.C. Pieper, J.E. Bowsher, M.P. Tornai, C.N. Archer, and R.J. Jaszczak. Parallel-beam tilted-head analytic SPECT reconstruction: Derivation and comparison with OSEM. *IEEE Trans. Nuc. Sci.*, 49:2394–2400, 2002.

[4] Eric W. Weisstein. "Gudermannian function". From *MathWorld*--A Wolfram Web Resource. http://mathworld.wolfram.com/GudermannianFunction.html

[5] J.E. Bowsher, M.P. Tornai, S.D. Metzler, J. Peter, and R.J. Jaszczak. SPECT breast imaging using more nearly complete orbits and combined pinhole-parallelbeam collimation. In *IEEE Nucl. Sci. Symp. & Med. Imag. Conf. Rec.*, volume 3, pages 1328–1330, 2001.

[6] S. D. Metzler, J. E. Bowsher, and R. J. Jaszczak. Geometrical similarities of the Orlov and Tuy sampling criteria and a numerical algorithm for assessing sampling completeness. *IEEE Trans. Nucl. Sci.*, 50(5):1550–1555, 2003.

[7] S.D. Metzler, J.E. Bowsher, M.P. Tornai, B.C. Pieper, J. Peter, and R.J. Jaszczak. SPECT breast imaging combining horizontal and vertical axes of rotation. *IEEE Trans. Nuc. Sci.*, 49(1):31–36, 2002.

[8] M. Defrise, R. Clack, and D.W. Townsend. Imaging reconstruction from truncated, two-dimensional, parallel projections. *Inverse Problems*, 11:287–313, 1995.

[9] H. K. Tuy. An inversion formula for cone-beam reconstruction. *SIAM J. Appl. Math.*, 43:546–552, 1983.

APPENDIX A

STATEMENT OF WORK

Task 1 Implement and characterize modified basis set of orbits (Months 1-5):

a. Implement dynamic ROR capability in hardware to enable fully computer controlled gantry. (Month 1)
b. Program gantry for: modified circle-plus-arc orbit with different arc locations, cloverleaf orbit. (Month 2)
c. Perform phantom measurements using modified orbits and evaluate projection data for signal-to-noise (SNR), contrast, and lesion visualization improvement. (Months 2-5).

Task 2 Development and investigation of novel orbits (Months 5-22):

a. Use Monte Carlo and Analytic computer simulations, including computations of Orlov Volumes, to develop novel orbits for various breast shapes and sizes through parameters of viewable breast volume, radius-of-rotation (ROR), camera tilt angle (to minimize background contamination). (Months 5-12)
b. Investigate the effect of additional bed shielding on positioning of the compact gamma camera. (Months 12-15)
c. Investigate acquisition and system parameters, including system tilt for axillary imaging, total number of projections and hence angular sampling, and distribution of the scan time. (Months 15-18)
d. Develop software to automate process of orbit creation, utilizing dynamic ROR control. (Months 18-22)

Task 3 Experimental evaluation of orbits (Months 22-36):

a. Acquire experimental projection data using cold rod and cold disk phantoms for resolution and sampling characterization, respectively. (Months 22-29)
b. Utilize anthropomorphic breast containing lesions and torso phantoms to acquire projection data. Analyze reconstructed images for contrast, signal-to-noise ratio, lesion detectability, and extent of artifacts caused by torso contamination. (Months 29-36)

APPENDIX B

EVALUATION OF 3D ACQUISITION ORBITS WITH AN EMISSION MAMMOTOMOGRAPHY SYSTEM INCORPORATING A FULL-FIELD CZT DETECTOR

C.N. Brzymialkiewicz[2], R.L. McKinley[1,2], and M.P. Tornai[1,2]

[1]Department of Radiology, Duke University Medical Center, Durham, NC 27710

[2]Department of Biomedical Engineering, Duke University, Durham, NC 27710

This work was supported by U.S. Army Grant No. DAMD17-03-1-0558 and by the National Institutes of Health, under grant R01-CA96821.

Abstract

Nuclear medicine based molecular imaging techniques can be used as an adjunct tool in the diagnosis of breast cancer. Dedicated breast single photon emission computed tomography (SPECT), with a compact, dedicated detector and unique hemispherical positioning gantry, allows for fully 3D tomographic acquisitions about the uncompressed breast. Our lab has recently incorporated a 16x20cm^2 quantized cadmium-zinc-telluride detector into our dedicated full-field emission mammotomography system. The LumaGEM 3200-S consists of 5120 segmented pixels, and utilizes a high resolution parallel-hole collimator. Complex acquisition trajectories have been developed that contour the breast, utilizing the unique capabilities of the gantry. In this work, circle-plus-arc (CPA) orbits are studied because they provide for extended viewing times in a specific quadrant of the breast, which may contain an indeterminate lesion suspected *a priori* from mammography studies. However, at certain camera positioning angles, the detector may view unscattered primary radiation from the heart and liver more directly, hence increasing background contamination. The effect on image quality of the azimuthal position of the arc in each of four quadrants, as well as the degree of the arc, is measured and compared. Additionally, because the spatial resolution characteristics of the CPA orbits are not uniform throughout the quadrants, a new orbit that is a combination of multiple overlapped CPA orbits is also implemented and investigated. Image quality is evaluated based on measurements of lesions in a breast phantom with an attached anthropomorphic torso, including lesion signal-to-noise ratios and contrasts. In the future, this prototype device will be combined with a digital x-ray detector, for combined uncompressed 3D breast SPECT/x-ray CT mammotomography.

I. Introduction

Nuclear Medicine based functional or molecular imaging techniques provide a secondary diagnostic tool when mammographic findings are inconclusive. There is a significant increase in the accuracy of breast imaging for the diagnosis of primary breast cancer when mammography and scintimammography are combined (Buscombe et al. 2001). Breast density does not affect the diagnostic accuracy of scintimammography, suggesting women with dense breasts may benefit most from this supplementary role (Khalkhali et al. 2002;

Coover et. al. 2004). The diagnostic accuracy may be further improved by utilizing a tomographic imaging approach (Wang et al. 1997; Singh and Mumcuoglu 1998; Metzler et al. 2001; Pieper et al. 2002), and specifically, by utilizing fully 3D hemispherical positioning of the detector about a pendant, uncompressed breast (Archer et al. 2003; Tornai et al. 2003).

Central to the compact emission mammotomography system developed in our lab (Archer et al. 2003; Tornai et al. 2003) is its gantry, which allows for a virtually infinite set of camera trajectories, or orbits, with which to acquire data about the breast. A simple vertical-axis-of-rotation orbit for a camera (Wang et al. 1997) with a parallel-hole collimator cannot image as much of the breast volume as an orbit that includes camera tilt; the furthest into the breast one can image without tilt is limited to a plane along the nipple-chest axis where the camera is adjacent to the torso. Thus, cameras with a thick edge further decrease the viewable breast volume. One main advantage of 3D orbits that utilize increased polar tilt is then an increased viewable breast volume, potentially into the chest wall region (Tornai et al. 2003). However, with increased tilt angle, the camera may directly view cardiac and hepatic regions, which could contribute primary background contamination to the 2D projection images of the breast.

The primary aim of this study is to determine the effectiveness of orbit design in eliminating or minimizing direct views of the heart and liver, thus minimizing background contamination and its subsequent degrading effect on image quality. We evaluate the effect of the azimuthal position of the arc, as well as the maximal degree of polar tilt of the arc, for the circle-plus-arc (CPA) orbit by assessing measured lesion signal-to-noise ratios (SNR) and contrasts in iteratively reconstructed images of lesions in an anthropomorphic breast phantom attached to a torso. One drawback of the CPA orbit, however, is that it does not provide uniform resolution characteristics throughout each breast quadrant; to overcome this potential limitation, the cloverleaf and inverse cloverleaf orbits are also implemented and evaluated.

II. Methods and Materials

A. Emission Mammotomography System Description

Previously, the Application Specific Emission Tomography (ASET) system utilized a 12x12 cm^2 field-of-view (FOV) photomultiplier-based NaI(Tl) gamma camera, described in detail elsewhere (Archer et al. 2003; Tornai et al. 2003). Here, a compact cadmium-zinc-telluride (CZT), intrinsic, high-Z, semiconductor detector with 2.5x2.5x6 mm^3 quantized elements (60x84 array) now serves as the imaging component (*LumaGEM*™ 3200-S camera, *Gamma Medica, Inc.*, Northridge, CA). It has been shown previously for scintimammography that utilizing a CZT detector improves system performance over conventional gamma cameras for detecting breast lesions (Mueller et al. 2003).

In this study, we utilize a parallel-beam collimator with hexagonally arranged holes (1.22 mm hole size flat-to-flat, 0.2 mm septa, and 25.4 mm height). The gantry (figure 1), consisting of a laboratory jack, a goniometric stage, and a rotation stage (M-EL120 jack, BGM200 goniometer, RV350 rotation stage, *Newport*

Corp., Irvine, CA) allows for variable radii-of-rotation (ROR), polar tilt angles, and rotational azimuthal motions, respectively, thus enabling positioning of the camera face at any point on the arbitrary sets of concentric hemispheres about the pendant, uncompressed breast. Data acquisition and gantry motion are synchronized through a software interface.

B. Orbits

Because the emission mammotomograph may be used as a secondary diagnostic device, the suspected lesion location may be known from the initial x-ray mammogram. With this prior knowledge, the CPA orbit could be tailored to the patient, positioning the arc along the quadrant containing the suspected lesion. First, we investigate the variation of the azimuthal location of the arc (θ) and the maximum polar tilt of the camera (ϕ) (figure 2) for CPA. Various azimuthal arc locations examined include θ=45°, 135°, 225°, and 315° (see figure 3 for how these arc locations relate to the torso). The basic notion for the cloverleaf orbit is to utilize the circle portion of CPA only, where each quadrant contains one circle segment; then, the envelope of projections that do not intersect the other lobes produces the 'cloverleaf' (Archer et al. 2002). The inverse cloverleaf orbit employs the same idea, in that a part of CPA is used. In this case, it is the arc that is projected into each quadrant; then, the orbit is modified so that the trajectory sweeps into each quadrant gradually. In all cases, the minimum polar tilt is 15°; the maximum polar tilts investigated are ϕ=30° and 45°. The significance of these orbits, in addition to minimization of background activity, is that they allow 3D imaging of a pendant breast while avoiding physical features or other hindrances from a patient during the acquisition.

Note that all of the orbits described herein can be implemented to meet Orlov's sampling criteria for sufficient data collection for activity reconstruction when the activity is fully within the camera's field-of-view (FOV) for each projection angle (Orlov 1975). However, in this set of experiments, the filled torso distal to the breast introduces background activity which is not uniformly in the FOV for each and every projection angle, hence, Orlov's criteria is not strictly met. Our design goal in each orbit implementation is then to maximize the viewable volume of the breast, placing the center-of-rotation (COR) as far inside the breast as practicable to image near the chest wall, while minimizing views that directly view the heart and liver. Due to complications in camera positioning, one sampling scheme involves implementing a variation of the CPA, in that, the minimum polar tilt is 15° (rather than 0° in a more strict application of Orlov's criteria); this implementation allows for the COR to be moved further into the breast by approximately 2cm.

The radius-of-rotation (ROR) is defined as the perpendicular distance between the center of the detector face and the COR. Given the geometry of a pendant breast and the tilts afforded by the system to contour the breast, proximity of different parts of the camera will vary with respect to the breast and an azimuthal axis of rotation. Orbits are designed to optimally contour the breast (examples given in figure 2), utilizing dynamic ROR control, allowing at most a 1cm distance between the camera face and the breast surface. The largest ROR used was 8cm.

C. Phantom Preparation and Image Acquisitions

Based on compiled, published data (Wackers et al. 1989; Maublant et al. 1996; Pani et al. 1998; Williams et al. 2000; Majewski et al. 2001), an anthropomorphic torso, heart, liver, breast (*RSD Inc.*, Newport Beach, CA) and lesions (*Data Spectrum Corp.*, Hillsborough, NC) (figures 3 and 4) were filled according to the concentration ratios given in Table 1. The breast phantom was custom made to our specifications, and is one of several phantoms of varying size and shape. We assume an initial total dose of 25mCi (925MBq), with the heart uptake of 1.2% after 5 minutes (Wackers et al. 1989). Because we are evaluating the acquisition orbit, the absolute activities were arbitrarily increased by a factor of 4, to ensure visualization and characterization of the lesions with the various sampling schemes.

A 9.5mm diameter lesion was placed centrally in the breast, and an 8mm diameter lesion was placed in the upper outer quadrant of the breast (figure 4). Total image time was adjusted to compensate for radioactive decay, with the initial scan acquired for 20 minutes providing count rates of ~0.2kcps. In all acquisitions, a symmetric ±4% window about the 140 keV photopeak of Tc-99m was used. While the imaging system will consist of a radio-opaque patient support bed, the phantoms were imaged without any shielding of the torso from the camera system, thus giving the worst possible contamination to the imaging system.

D. Reconstruction and Image Analysis

Data were reconstructed using a ray driven ordered subsets expectation maximization (OSEM) with eight subsets, five iterations, attenuation correction, and 2.5mm voxels. A three-dimensional Hann filter was applied to the reconstructed data with a cutoff of 0.7 times the Nyquist frequency. Regions-of-interest (ROIs) were drawn both inside the lesions and circumferentially about each lesion in the breast background. For the 9.5mm lesion, a twelve pixel ROI was used, with 24 separate background regions drawn about the lesion in the same slice, two slices above, and two slices below, totaling 288 background pixels. For the 8mm lesion, a nine pixel ROI was drawn, again with 24 background regions with the same ROI pixel size, for a total of 216 pixels. SNR was calculated as $(ROI_{lesion}-ROI_{breast})/\sigma_{breast}$, where ROI_{lesion} and ROI_{breast} are the mean values of the counts within each respective region and σ_{breast} is the standard deviation of the breast background; contrast is defined as $(ROI_{lesion}-ROI_{breast})/ROI_{breast}$.

III. Results

Both the 9.5mm and 8mm lesions are visible for all acquired orbits. A few representative reconstructed images are presented in figure 5. When using any degree of tilt, increasing the tilt angle does not significantly increase the viewable breast volume, yet, with increased polar tilt, more background contamination can be seen (compare CPA $\phi=30°$, and CPA $\phi=45°$, both with an arc location of $\theta=225°$). For particular combinations of polar and azimuthal locations of the detector, considering the normalized and decay corrected counts within the photopeak energy window, a distinct asymmetry results that is directly related to the increased counts from the torso. SNR and contrast values for the second OSEM iteration for both the 9.5mm and 8mm lesions are given in Table 2. Considering the centrally placed lesion alone, for a polar tilt of 30°, an arc location of 315° provides for the highest SNRs and contrasts, approximately twice as high as when the arc is located at 225°. With increased tilt, for an arc location of 315°, contrasts remain about the same, yet SNRs are slightly worse. For the smaller, 8mm lesion, CPA $\phi=30°$, $\theta=135°$ performs the best, suggesting the circle portion of the orbit may be more important in orbit design than the arc, in terms of total scan time near the lesion. The newly implemented inverse cloverleaf, for a polar tilt of 45°, (which capitalized on the arcs of CPA) has the highest SNRs and contrasts for all polar tilts and all azimuthal locations for the centrally located 9.5mm lesion; but, for the peripherally located 8mm lesion, the inverse cloverleaf was one of the worst-performing orbits.

IV. Discussion and Conclusions

The results indicate a strong dependence on both polar tilt angle and azimuthal arc location on image quality. These two parameters cannot be considered independently when designing an orbit. In some cases, increased polar tilt improves SNR and contrast values, while in others it decreases these values; no single camera trajectory will equally optimize image quality when considering various lesions sizes and locations. However, because of the flexibility of the system and the potential *a priori* suspected lesion location from mammography, an orbit can be tailored to each patient to maximally view the breast volume while maintaining proximity to the breast, increasing scan time near the suspected lesion while minimizing views of the heart and liver. Furthermore, given modest patient (torso) shielding with a radio-opaque support bed, the background activity could be reduced, which should yield improvements in the measured SNRs and contrasts, or perhaps reduce the relative differences and variability as measured here without any background shielding; this remains to be implemented and investigated since patients will more likely be scanned under those conditions. Ultimately, this emission component of the ASET system will be combined with a compact, dedicated breast x-ray CT mammotomography scanner, for further improved imaging of the breast.

Acknowledgments

The authors thank J. Li, K. Parnham, B. Patt (*Gamma Medica*) for their assistance with camera operation, T.G. Turkington for use of SPECTER 4.0 for visual display and analysis, and J.E. Bowsher for access to and invaluable help with the OSEM reconstruction. One coauthor, MPT, is a scientific advisor to *Gamma Medica*.

References

Archer, C.N., M.P. Tornai, J.E. Bowsher, M.L. Bradshaw. 2002. Initial Investigation of Circle-Plus-Arc Orbit Variants with a Dedicated Emission Mammotomograph. *IEEE Conf. Rec. Nucl. Sci. Symposium & Med. Imag. Conf.* no. 2, pp. 1118–1122.

Archer, C.N., M.P. Tornai, J.E. Bowsher, S.D. Metzler, B.C. Pieper, and R.J. Jaszczak. 2003. Implementation and Initial Characterization of Acquisition Orbits About a Pendulous Breast Using the ASET System. *IEEE Trans. Nucl. Sci.*, vol. 50, no. 3, pp. 413–420.

Bowsher, J.E., D.R. Gilland, C.E. Floyd, R.J. Jaszczak, V.E. Johnson, and R.E. Coleman. 1992. Three Dimensional Iterative Reconstruction for SPECT. *J. Nucl. Med.*, vol. 33, pp. 879.

Buscombe, J. R., J. B. Cwikla, B. Holloway, and A. J. W. Hilson. 2001. Prediction of the Usefulness of Combined Mammography and Scintimammography in Suspected Breast Cancer Using ROC Curves. *J. Nucl. Med.,* vol. 42, pp. 3–8.

Coover, L.R., G. Caravaglia, and P. Kuhn. 2004. Scintimammography with Dedicated Breast Camera Detects and Localizes Occult Carcinoma. *J. Nucl. Med.,* vol. 45, pp. 553–558.

Khalkhali, I., J. K. Baum, J. Villaneuva-Meyer, S. L. Edell, L. G. Hanelin, C. E. Lugo, R. Taillefer, L. M. Freeman, C. E. Neal, A. M. Scheff, J. L. Connolly, S. J. Schnitt, M. J. Houlihan, J. S. Sampalis, and S. B. Haber. 2002. 99mTc Sestamibi Breast Imaging for the Examination of Patients with Dense and Fatty Breasts: Multicenter Study. *Radiology*, vol. 222, pp. 149–155.

Majewski, S., D. Kieper, E. Curran, C. Keppel, B. Kross, A. Palumbo, V. Popov, A. G. Weisenberger, B. Welch, R. Wojcik, M. B. Williams, A. R. Goode, M. More, and G. Zhang. 2001. Optimization of Dedicated Scintimammography Procedure Using Detector Prototypes and Compressible Phantoms. *IEEE Trans. Nucl. Sci.*, vol. 48, no. 3, pp. 822–829.

Maublant, J., M. de Latour, D. Mestas, A. Clemenson, S. Charrier, V. Feillel, G. Le Bouedec, P. Kaufmann, J. Dauplat and A. Veyre. 1996. Technetium-99m-Sestamibi Uptake in Breast Tumor and Associated Lymph Nodes. *J. Nucl. Med.*, vol. 37, no. 6, pp. 922–925.

Metzler, S.D., J.E. Bowsher, M.P. Tornai, B.C. Pieper, J. Peter, and R.J. Jaszczak. 2002. SPECT Breast Imaging Combining Horizontal and Vertical Axes of Rotation. *IEEE Trans. Nuc. Sci.,* vol. 49, no. 1, pp. 31–36.

Mueller, B., M. K. O'Conner, I. Blevis, D. J. Rhodes, R. Smith, D. A. Collins, and S. W Phillips. 2003. Evaluation of a Small Cadmium Zinc Telluride Detector for Scintimammography. *J. Nucl. Med.*, vol. 44, pp. 602–609.

Orlov, S.S. 1975. Theory of Three Dimensional Reconstruction. *Sov. Phys. Crystallogr.*, vol. 20, no. 3, pp. 312–314.

Pani, R., G. De Vincentis, F. Scopinaro, R. Pellegrini, A. Soluri, I.N. Weinberg, A. Pergola, R. Scafe, and G. Trotta. 1998. Dedicated Gamma Camera for Single Photon Emission Mammography (SPEM). *IEEE Trans. Nucl. Sci.,* vol. 45, no. 6, pp. 3127–3133.

Pieper, B.C., J.E. Bowsher, M.P. Tornai, J. Peter, and R.J. Jaszczak. 2001. Breast Tumor Imaging Using Tiltable Head SPECT Cameras. *IEEE Trans. Nuc. Sci.*, vol. 48, no. 4, pp. 1477—1492.

Singh, M. and E. Mumcuoglu. 1998. Design of a CZT Based BreastSPECT System. *IEEE Trans. Nuc. Sci.*, vol. 45, no. 3, pp 1158–1165.

Tornai, M.P., J.E. Bowsher, C.N. Archer, J. Peter, R.J. Jaszczak, L.R. MacDonald, B.E. Patt, and J.S. Iwanczyk. 2003. A 3D Gantry Single Photon Emission Tomograph with Hemispherical Coverage for Dedicated Breast Imaging. *Nucl. Inst. Meth.*, vol. A497, no. 1, pp. 157–167.

Williams, M. B., D. Narayanan, M. J. More, P. J. Goodale, S. Majewski, and D. A. Kieper. 2003. Analysis of

Position-Dependent Compton Scatter in Scintimammography with Mild Compression. *IEEE Trans. Nucl. Sci.*, vol. 50, no. 5, pp. 1643–1649.

Wackers, F. J. Th., D. S. Berman, J. Maddahi, D. D. Watson, G. A. Beller, H. W. Strauss, C. A. Boucher, M. Picard, B. L. Holman, R. Fridrich, E. Inglese, B. Delaloye, A. Bischof-Delaloye, L. Camin, and K. McKusick. 1989. Technetium-99m Hexakis 2-Methoxyisobutyl Isonitrile: Human Biodistribution, Dosimetry, Safety, and Preliminary Comparison to Thallium-201 for Myocardial Perfusion Imaging. *J. Nucl. Med.*, vol. 30, no. 3, pp. 301–311.

Wang, H., C. Scarfone, K. L. Greer, R. E. Coleman, and R. J. Jaszczak. 1997. Prone Breast Tumor Imaging Using Vertical Axis-of-Rotation (VAOR) SPECT Systems: An Initial Study. *IEEE Trans. Nucl. Sci.*, vol. 44, no. 3, pp. 1271–1276.

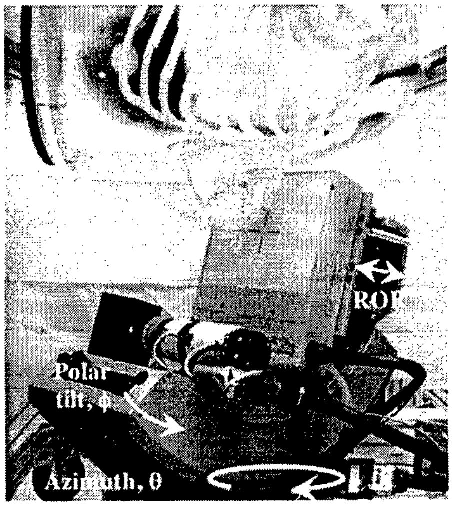

Figure 1. Photograph of the dedicated emission mammotomography system with 16x20 cm^2 FOV CZT-based LumaGEM3200S™. Azimuthal, polar, and radial controls provide for fully 3D data acquisition. A filled anthropomorphic torso phantom and pendant, uncompressed 1060ml breast are suspended within the camera's FOV. (B&W photo could be provided for publication, as necessary)

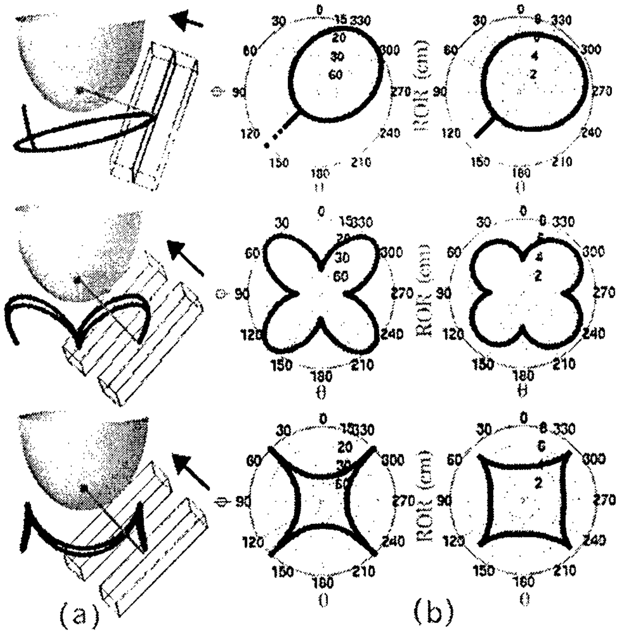

Figure 2. Scale schematics of measured orbits. From top to bottom: Circle-Plus-Arc (CPA), with 45° polar tilt (φ) and 135° azimuthal arc location (θ) shown; Cloverleaf (Cloverleaf); Inverse Cloverleaf (InvCloverleaf). In (**a**), the wire-frame box represents our 16x20 cm^2 CZT detector, with center on the trajectory about the breast (dotted black path). Solid gray line extending from the center-of-rotation through the breast (COR located ~2cm inside the breast, along the nipple-chest axis) is perpendicular to the detector face. Note that while azimuthal and polar angles are designed to more-nearly meet complete sampling requirements, ROR contouring allows for the camera to move close to the breast (see black arrow, with second, closer proximity detector). (**b**) Example set of polar plots for 45° maximum polar tilt, of: (LEFT) azimuthal angle (θ) (plotted around the circle from 0° to 360°) versus polar tilt (φ) (plotted as a radius, with 90° at center and 0° at edge); (RIGHT) azimuthal angle (θ) versus contouring ROR (radius from center).

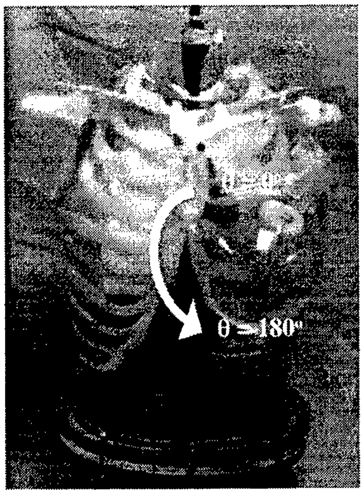

Figure 3. Photograph of the upright positioned torso phantom, with labeled detector azimuth location relative to the pendant, uncompressed breast. Note also the (color and radioactivity) filled heart and liver. (B&W photo could be provided for publication, as necessary)

Figure 4. Photograph (superior view) of the 1060ml anthropomorphic breast phantom with two lesions. Dimensions in the medial-lateral (ML), and nipple-chest (NC) directions as labeled; superior-inferior dimension is 15.9cm. One 9.5mm diameter lesion and one 8mm diameter lesion were inserted into the breast as shown. The 9.5mm lesion was placed in the center of the breast, ~5cm from the chest wall. The 8mm lesion was placed in the upper outer quadrant, the quadrant for which the probability of a lesion being present is the highest. Lesions have an absolute activity concentration ratio of 2 μCi/ml. (B&W photo could be provided for publication, as necessary)

Table 1. Activity concentration ratios for each of the filled organs in the anthropomorphic torso and breast phantoms.

Organ	**Volume (ml)**	**Concentration (μCi/ml)**	**Ratio**
Breast	1060	0.3	1
Torso	7810	0.3	1
Liver	1010	4.2	12.7
Heart (outer wall)	290	4.0	12.2
Lesions: (1cm diameter)	0.43	2.0	6
(8mm diameter)	0.26	2.0	6

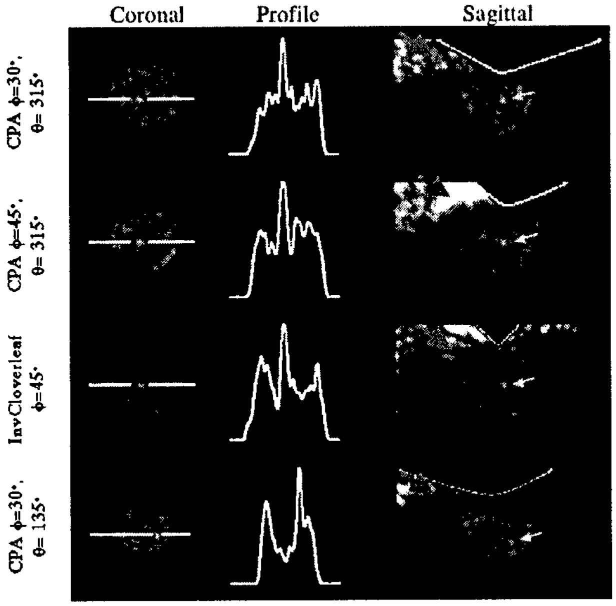

Figure 5. OSEM reconstructed data (8 subsets; 2^{nd} iteration shown; 2.5mm voxel size; post-reconstruction 3D Hann filter applied with a cutoff of 0.7 times the Nyquist frequency). Representative images were chosen to illustrate the effect of increasing polar tilt with respect to background contamination for the CPA orbits, and from the orbits which yield the highest overall SNR and contrast values for the 9.5mm and 8mm lesions (InvCloverleaf ϕ=45° and CPA ϕ=30°, θ=135°, respectively, see Table 2). Profiles are drawn through the 9.5mm lesion for all but CPA ϕ=30°, θ=135°, which is shown through the 8mm lesion. Orange arrows point to the background contamination from the torso, heart, and liver. Yellow arrows point to the 9.5mm lesion for the first three orbits; yellow arrow points to the 8mm lesion in the bottom orbit.

Table 2. SNR and contrast values as determined from ROIs drawn inside the lesions and over the breast background (2^{nd} iteration).

Orbit	**9.5 mm diameter (0.43 ml) lesion**		**8 mm diameter (0.26 ml) lesion**	
	SNR	Contrast	SNR	Contrast
CPA 30, 45	4.9	0.9	2.3	0.3
CPA 30, 135	5.1	0.6	6.3	0.7
CPA 30, 225	3.2	0.6	2.9	0.5
CPA 30, 315	5.8	1.0	4.1	0.6
Cloverleaf 30	4.1	0.6	3.8	0.5
Inverse Cloverleaf 30	3.2	0.5	5.0	0.6
CPA 45, 45	5.9	0.9	1.8	0.2
CPA 45, 135	3.8	0.7	4.3	0.6
CPA 45, 225	4.8	1.0	5.5	0.6
CPA 45, 315	4.9	1.0	4.0	0.4
Cloverleaf 45	3.7	0.8	2.0	0.3
Inverse Cloverleaf 45	6.3	1.2	1.2	0.2

APPENDIX C

3D Data Acquisition Sampling Strategies for Dedicated Emission Mammotomography for Various Breast Sizes

Caryl N. Brzymialkiewicz[1,2], Martin P. Tornai[1,2], Randolph L. McKinley[1,2], James E. Bowsher[2]

Department of Biomedical Engineering, Duke University, Durham, NC 27710
Department of Radiology, Duke University Medical Center, Durham, NC 27710

The dedicated emission mammotomography system developed in our lab is in preparation for initial patient studies. As a preliminary step, we evaluate the effect of various breast sizes on this paradigm. The hemispherical positioning gantry allows ample flexibility in sampling a pendant, uncompressed breast. Recently acquired, realistic anthropomorphic torso (which includes the upper portion of the arm) and breast phantoms emphasize the necessity of employing unique camera trajectories (orbits). Several novel 3D orbits have been implemented with fully contoured radius-of-rotation capability to compensate for the positioning demands that are required for different breast sizes; while a general orbit design may remain the same between two different breasts, the absolute polar tilt range and ROR range may vary. Here, we choose to satisfy Orlov's sampling condition for tomographic orbits by placing the center-of-rotation as far into the breast as practicable to maximize the viewable breast volume without sacrificing more-nearly complete sampling. The system utilizes a 16x20 cm^2 CZT-based compact gamma camera with 2.5mm^2 pixels. We evaluate image quality, in terms of lesion signal-to-noise ratio and contrast, for several lesion sizes (5mm-10mm diameter) utilizing several concentration ratios (3:1 to 10:1), embedded in various size breast phantoms (volumes ranging from 240ml to 1730ml). These ranges facilitate evaluation of robustness of sampling methods across all cases.

This work is supported by U.S. Army Grant No. DAMD17-03-01-0558 and NIH grant R01-CA96821.

Submitted May 19, 2004 to IEEE MIC, to be held in Rome, Italy in October 2004
Accepted for poster presentation

APPENDIX D

Evaluation of Fully 3D Emission Mammotomography with a Compact Cadmium Zinc Telluride Detector

Caryl N. Brzymialkiewicz, *Member, IEEE*, Martin P. Tornai, *Member, IEEE*,
Randolph L. McKinley, *Member, IEEE*, and James E. Bowsher, *Member, IEEE*

Abstract

A compact, dedicated cadmium zinc telluride (CZT) gamma camera coupled with a fully three-dimensional acquisition system may serve as a secondary diagnostic tool for imaging of breast cancers, particularly in cases when mammographic findings are inconclusive. The key components of the emission mammotomography system developed in our lab are a 16x20 cm^2 quantized CZT detector and 3D positioning gantry, which allows for an infinite number of camera trajectories within concentric hemispheres about a pendant, uncompressed breast. The intrinsic spatial resolution, energy resolution, and sensitivity of the detector are evaluated with Tc-99m filled flood sources, capillary line source measurements, and a frequency-resolution phantom. The detector has a measured intrinsic energy resolution of 8.0% FWHM at 140 keV. Planar spatial resolution measurements matched well with predicted values. In reconstructed mini-rod data, given a 4.4 cm radius-of-rotation, the 3.1 mm diameter rods are discernible. Two different breast phantom shapes and sizes (935 and 1060 ml), and three different lesion sizes (9.5, 8, and 5 mm diameter) are used to evaluate the system for 3D mammotomography. Orbits are designed to optimize the viewable breast volume while more-nearly-sufficiently sampling the breast. Image quality is evaluated with signal-to-noise ratios and contrasts of the lesions, both with and without additional torso phantom background. Results indicate 3D mammotomography, incorporating a compact CZT detector, may be a promising dedicated breast imaging technique for visualization of tumors <1 cm in diameter.

Index Terms

Breast imaging, emission mammotomography, single photon emission computed tomography, three-dimensional orbits, CZT detector

I. INTRODUCTION

COMPACT, dedicated gamma cameras coupled with a fully three-dimensional acquisition system can serve as a secondary diagnostic tool for imaging of breast cancers, particularly in cases when mammographic findings are inconclusive. The significance of a compact camera in single photon emission imaging is its ability to facilitate closer proximity imaging, thus minimizing distance-dependent sensitivity and spatial resolution limitations. Utilizing planar imaging alone, there is a significant increase in the accuracy of breast imaging for the diagnosis of primary breast cancer when mammography and scintimammography are combined [1]. An advantage of employing nuclear medicine techniques stems from the fact that the accuracy of scintimammography is unaffected by breast density: studies have shown women with dense breasts may benefit most from this complementary imaging technique [2], [3]. Thus, several groups have investigated compact position-sensitive photomultiplier tube (PSPMT)-based gamma cameras for the breast-imaging paradigm [4]-[7].

While these dedicated PSPMT cameras offer an improvement over clinical gamma cameras, the energy discrimination can be further improved by using cadmium zinc telluride (CZT) semiconductor detectors. Scatter rejection will play an important role in the breast-imaging paradigm where cardiac and hepatic background can contaminate the primary lesion signal [8], [9]. The use of CZT detectors for the detection of lesions has been previously proposed and investigated through simulation studies using SPECT [10] and scintimammography measurements [11].

Applying a tomographic approach may improve the diagnostic accuracy even further over that given currently by combining scintimammography and mammography, considering that the contrast will improve with such a 3D

TMI SUBMISSION DEADLINE: Manuscript submitted July 15, 2004. This work was supported by U.S. Army Grant No. DAMD17-03-1-0558 and by the National Institutes of Health under grant R01-CA96821.

C.N. Brzymialkiewicz, M.P. Tornai, and R.L. McKinley are with the Departments of Biomedical Engineering and Radiology; J.E. Bowsher is with the Department of Radiology, Duke University Medical Center, Durham, NC 27710 USA (email:cnb3@duke.edu).

technique. In addition, the 3D localization of the tumor is provided. Dedicated breast SPECT imaging has been investigated both with clinical gamma cameras and dedicated systems [8]-[10], [12]-[18]. Our group has previously demonstrated that a compact, fully 3D hemispherical positioning gantry that allows for positioning of the detector anywhere about a pendant, uncompressed breast may significantly improve image quality [8], [9]. These studies were performed with quantized NaI(Tl) scintillator, PSPMT-based compact gamma cameras.

A key component of the fully 3D acquisition system developed by our group is the hemispherical gantry, allowing several degrees of freedom to position the camera anywhere about a pendant, uncompressed breast. Thus, the techniques presented here can also directly be applied to other imaging modalities, including cone-beam x-ray transmission imaging. There is an infinite set of camera trajectories, or orbits, with which to acquire data. A simple vertical-axis-of-rotation orbit for a camera [12] with a parallel-hole collimator yields a smaller viewable breast volume than an orbit which includes camera tilt, due to positioning restraints imposed by the detector; the furthest into the breast one can image without tilt is limited to the plane along the nipple-chest axis where the camera is adjacent to the torso. Cameras with a thick edge further decrease the viewable breast volume. One main advantage of fully-3D orbits that utilize increased polar tilt is an increased viewable breast volume, potentially into the chest wall region [8]. However, with increased tilt angle, the camera may directly view cardiac and hepatic regions, which could contribute primary background contamination to the 2D projection images of the breast.

The primary aim of this study is to evaluate the ability of the emission mammotomography system using a compact CZT detector to image lesions in a uniform breast background, both with and without additional torso backgrounds. To our knowledge, this is the first implementation and evaluation of a fully developed CZT detector and system for dedicated tomographic imaging of the breast.

II. PERFORMANCE CHARACTERISTICS OF THE CZT DETECTOR: METHODS AND RESULTS

The LumaGEM^{TM} 3200-S camera (*Gamma Medica Inc.*, Northridge, CA) (Fig. 1) utilizes a 60x84 array of 2.5x2.5x6 mm^3 quantized elements. The detector is kept at 15°C, using water cooling. Of the detector's 5120 pixels, 99.8% were usable in this set of experiments. We evaluated the camera with a parallel beam collimator with hexagonally arranged holes (1.22 mm hole size flat-to-flat, 0.2 mm septa, 25.4 mm height). The measured uniformity of the detector was ±4.0%.

The energy resolution was measured using a flood source of Tc-99m for 10M total counts, with count rates of ~5.8 kcps using an open energy window. The gain balanced, summed energy spectra (Fig. 2) yielded an intrinsic energy resolution of 8.0% full-width half-maximum (FWHM) at 140 keV. Using the same protocol for calculation of the FWHM (as per [19]) for each individual pixel also resulted in a mean intrinsic energy resolution of 8.0%, with a range of 4.8% to 33.1% (Fig. 2, histogram).

Sensitivity, defined as (counts/sec)/mCi, was measured with a 14 cm diameter petri dish filled with an ~3 mm layer of 9.9 mCi Tc-99m, placed 10 cm from the collimator face. The dose calibrator in our lab has a ±5% error. The sensitivity measurement is based on a symmetric ±8% energy window, which is the width used for several of the phantom studies. The time needed to collect a total of 4M counts was recorded. The measured sensitivity of the system for the parallel-beam collimator using Tc-99m was 804 cps/mCi (21.7 cps/MBq).

Planar spatial resolution was measured by acquiring images of a single capillary tube, filled with 4.5 mCi of Tc-99m in 5.5 cm of its length. Projection data were acquired with the line source placed both horizontally and vertically with respect to the camera, at a collimator-source distance of 1 through 9 cm. A 15% asymmetric (-5+10%) energy window about the 140 keV photopeak was used for all acquisitions. Planar spatial resolution plotted as a function of distance to the detector, as measured with the capillary line source, compared well to the expected resolution calculated from the Anger equations (Fig. 3). Horizontal and vertical measurements may be different due to the line source being ideally aligned with the collimator holes in one case, and/or non-alignment with the Cartesian distribution of the quantized CZT elements.

Reconstructed spatial resolution was determined from SPECT measurements of two capillary tubes, each filled with 3.2 mCi of Tc-99m in 5.5 cm, suspended along the vertical axis of rotation with one placed in the center and one offset by 2 cm. Again, a 15% asymmetric (-5+10%) window was used. Simple circular tomography over 360° was used for these measurements with 128 projections, at 5 sec/projection. Acquisitions were acquired at rotation radii of 3, 5, and 7 cm. Note that the radius-of-rotation (ROR) is defined as the perpendicular distance between the center of the detector face and the center-of-rotation (COR). Images were reconstructed from projection data

TABLE I

ORBIT PARAMETERS USED FOR EACH BREAST PHANTOM ACQUISITION, WITH ALL ORBITS ACQUIRED OVER A 360° AZIMUTHAL RANGE (θ).

Orbit Name	Acronym	ϕ Range (min-max)	ROR Range (min-max)	Number of Projections
935 ml Breast, COR located at nipple				
Tilted-Parallel-Beam	TPB	45°	1.9 - 3.7	128
Circle-Plus-Two-Arcs	CP2A	0 - 45°	1.9 - 9.3	162
Circle-Plus-Arc	CPA	0 - 45°	2.4 - 9.3	145
Cloverleaf	CLOVER	0 - 45°	2.0 - 9.3	268
Inverse Cloverleaf	invCLOVER	0 - 45°	2.0 - 9.3	268
1060 ml Breast + Filled Torso, COR located ~2 cm inside nipple				
Tilted-Parallel-Beam	TPB	45°	3.2 - 4.4	128
Circle-Plus-Arc	CPA	15 - 45°	3.8 - 7.1	139
Cloverleaf	CLOVER	15 - 45°	3.6 - 7.2	256
Inverse Cloverleaf	invCLOVER	15 - 45°	3.6 - 7.1	256

using an ordered subsets expectation maximization (OSEM) algorithm [20], [21] implemented with a ray-tracing capability with 8 subsets, 5 iterations, and 2.5 mm voxels. SPECT spatial resolution results are shown in Fig. 4.

A 7.7 cm diameter cylinder containing a resolution-frequency phantom consisting of mini-acrylic rods each 2.6 cm long (model ECT/DLX/MP, *Data Spectrum Corp.*, Hillsborough, NC) was used as another measure of the spatial resolution of the system (Fig. 5). The rods in each of six sectors had equal diameters of 4.7, 3.9, 3.1, 2.3, 1.5 and 1.1 mm, spaced on twice their diameter. Water containing 15.6 mCi of Tc-99m filled the interstitial spaces between the rods. The phantom was oriented such that the rods were vertical, parallel to the axis of rotation. The camera and phantom were both leveled, and the rods were placed in the central portion of the field-of-view (FOV). The ROR was fixed at 4.4 cm. Simple circular tomography was used for these measurements with 256 projections over 360° and an acquisition time of 28 seconds per projection. A ±8% energy window was used, yielding count rates of ~5.9 kcps.

Reconstructed results with 8 subsets, 20 iterations, and 2.5 mm voxels, from the mini-rod measurements are shown in Fig 5. The second sector of rods (3.9 mm diameter) are clearly distinguishable, as would be expected with results from Figs. 3 and 4 given the ROR of 4.4 cm. The 3.1 mm rods are also discernible; though the profile reveals a relatively low contrast, the rods can indeed be resolved.

III. 3D MAMMOTOMOGRAPHY

A. Methods

The significance of any 3D orbit with a dedicated system is that it allows for fully-3D imaging of an uncompressed, pendant breast while facilitating the avoidance of physical features or other hindrances from a patient during the acquisition. The tomographic gantry (Fig. 6) used to position the camera center at any point in a hemispheric bowl about the COR has been previously described [8], [9]. A basis set of orbits was initially characterized using a smaller, 12.8x12.8 cm^2 FOV NaI(Tl) camera incorporated onto the dedicated emission mammotomograph [9]. While results showed significant improvements in contrasts and signal-to-noise ratios (SNRs) for breast lesions as compared to simple vertical-axis-of-rotation acquisitions and uncompressed planar imaging, the system was limited by the relatively small FOV. Image artifacts resulted from a necessary camera shift to compensate for larger truncated breast volumes. The larger FOV provided by the current CZT detector obviates this shift. Thus, in this work, we evaluate a subset of orbits from [9] here acquired with the full FOV CZT detector, in addition to evaluating newer orbits. Ideally, an acquisition orbit should: (1) meet Orlov's sampling criterion for sufficient data collection for accurate reconstruction of the activity distribution within the breast when the activity is fully within the camera's FOV for each projection angle [22]; (2) maximize the viewable breast volume; (3) minimize the background contamination from cardiac and hepatic sources; and (4) contour the breast to minimize the distance related resolution degradations.

As a secondary diagnostic tool, the emission mammotomography system evaluated here can image an indeterminate lesion which may have presented on an initial mammogram. Orbits can be designed to contour the breast keeping the detector position near such a lesion. Thus, for this set of experiments, we examine those illustrated

TABLE II

DIMENSIONS OF THE CUSTOM BREAST PHANTOMS.

Breast Volume (ml)	Dimensions (in cm) Superior-Inferior	Nipple-Chest	Medial-Lateral
935	20	7.5	15
1060	16	12	18

TABLE III

ACTIVITY CONCENTRATION RATIOS FOR EACH OF THE FILLED ORGANS IN THE ANTHROPOMORPHIC TORSO AND BREAST PHANTOMS.

Organ	Volume (ml)	Concentration (μCi/ml)	Ratio
Breast	1060	0.33	1.0
Torso	7810	0.33	1.0
Liver	1010	4.2	12.7
Heart (outer wall)	290	4.0	12.1
9.5 mm diam. lesion	0.43	2.0	6.1
8.0 mm diam. lesion	0.26	2.0	6.1

in Fig. 7(a). Given the geometry of a pendant breast and the tilts afforded by the system to contour the breast, proximity of different parts of the camera will vary with respect to the breast and an azimuthal axis of rotation. Orbits are designed to optimally contour the breast utilizing dynamic ROR control (example given in Fig. 7(b), ROR Ranges given in Table I), allowing at most a 1 cm separation between the camera's center and the breast surface.

While this work focuses on parallel-beam imaging utilizing a focal spot at infinity, Orlov's sampling criteria have been shown to be a special case [23] of Tuy's condition for cone-beam sampling [24], which outlines criteria for cone-beam type collimation geometries that are also possible with our system. The flexibility of the gantry allows for investigation of various sampling schemes, for a variety of converging or even diverging collimation beam configurations.

1) Isolated Breast Phantom: Two lesions, one 8 mm and one 5 mm inner diameter (*Data Spectrum Corp.*) were inserted into a ~935 ml custom-built, fillable anthropomorphic breast phantom (*Radiology Support Devices Inc.*, Newport Beach, CA) as shown in Fig. 8. The 8 mm lesion was placed centrally in the breast, while the 5 mm lesion was placed proximally (Fig. 8). The custom-made breast phantom is one of several, each with varying sizes and shapes; this particular model has dimensions as given in Table II. The dimensions of these phantoms are within the ranges measured in [25]. The lesion:breast radionuclide concentration ratio was 9.8:1, with an absolute lesion activity concentration of 12.1 μCi/ml. The initial scan was acquired for 20 minutes, with subsequent acquisitions adjusted to compensate for radioactive decay. A ±8% symmetric energy window about the 140 keV photopeak was used, yielding count rates of ~0.9 kcps. The breast phantom was attached to the anthropomorphic torso phantom to simulate complications in patient positioning, but the torso was *not* filled with radioactivity. This situation may indeed be similar to the intended breast imaging with a patient lying on a shielded, radio-opaque bed.

2) Breast Phantom with Filled Torso Background: To more nearly simulate a clinical study and thus match the biodistribution of activity in a patient, an anthropomorphic torso phantom containing a heart, liver, and lungs (*RSD Inc.*) was filled according to compiled, published data [4],[5],[26]-[29]. The breast phantom, torso and organs were filled according to the concentration ratios given in Table III, assuming an initial total dose of 25 mCi (925 MBq), with the heart uptake of 1.2% after 5 minutes [29].

Two lesions, one 9.5 mm and one 8.0 mm inner diameter (*Data Spectrum Corp.*) were also filled according to the concentration ratios given in Table III. The 9.5 mm lesion was placed centrally in the breast, while the 8 mm lesion was placed in the upper outer quadrant of the breast (Fig. 8). Total image time was adjusted to compensate for radioactive decay, with the initial scan acquired for 20 minutes. In all acquisitions, a symmetric ±4% window about the 140 keV photopeak of Tc-99m was used, providing count rates of ~0.2 kcps.

For the 3D camera trajectories implemented in these breast+filled torso experiments, the filled torso distal to the breast introduces background activity which is not uniformly in the FOV for each and every projection angle. Hence, Orlov's criteria is not strictly met. Thus, a design goal in this case is to maximize the viewable volume of

TABLE IV

MEASURED SNRS AND CONTRASTS, AT 2ND OSEM ITERATION.

	Lesion Size					
	9.5 mm (0.43 ml)		8 mm (0.26 ml)		5 mm (0.06 ml)	
Orbit	SNR	Contrast	SNR	Contrast	SNR	Contrast
935 ml Breast, 10:1 activity ratio, 12.1μCi/ml in lesions, 16% EWin						
			central		distal	
TPB	–	–	19.3	2.0	2.7	0.2
CP2A	–	–	26.6	1.9	4.9	0.2
CPA	–	–	17.3	1.4	3.9	0.2
CLOVER	–	–	23.2	1.4	7.9	0.3
invCLOVER	–	–	17.1	1.5	6.9	0.3
1060 ml Breast + Filled Torso, 6.1:1:12 activity ratio, 2.0μCi/ml in lesions, 8% EWin						
	central		distal			
TPB	4.6	0.8	3.4	0.5	–	–
CPA	4.8	1.0	5.5	0.6	–	–
CLOVER	3.7	0.8	2.0	0.3	–	–
invCLOVER	6.3	1.2	1.2	0.2	–	–

the breast by locating the COR as far inside the breast as practicable to image near the chest wall. Specifically, these orbits have a minimum polar tilt of 15°, with the exception of TPB (which maintains a 45° polar tilt) (Table I).

3) Image Reconstruction and ROI Analysis: Images were again reconstructed from projection data using the OSEM algorithm with ray-tracing capability, with 8 subsets, 5 iterations, calculated attenuation correction assuming a uniform emission volume, and 2.5 mm voxels. A 3D Hann filter with a cutoff of 0.7 times the Nyquist frequency was applied to the reconstructed data.

Regions-of-interest (ROIs) were drawn both inside the lesions and circumferentially about each lesion in the breast background. For lesion sizes of 9.5, 8, and 5 mm diameter, ROIs contained 12, 9, and 4 pixels, respectively. In all cases, 24 separate background regions were drawn about each lesion, 8 each in the slice containing the lesion's centroid, one 2.5 mm slice above, and one 2.5 mm slice below. The size of the background ROIs drawn about each lesion corresponded to the size of the ROI drawn within that lesion (e.g., for the 9.5 mm lesion, 24 background regions totaled 288 pixels, whereas for the 8 mm lesion, 24 background regions totaled 216 pixels).

The SNR was measured as the difference in mean pixel values of the lesion and breast background, divided by the standard deviation of the uniform background ($(\mathrm{ROI}_{lesion}\text{-}\mathrm{ROI}_{breast})/\sigma_{breast}$), where ROI_{lesion} and ROI_{breast} are the mean values of the counts within each respective region and σ_{breast} is the standard deviation of the uniform breast background. Lesion contrast is defined as the signal difference divided by the background signal ($(\mathrm{ROI}_{lesion}\text{-}\mathrm{ROI}_{breast})/\mathrm{ROI}_{breast}$).

B. Results

1) Isolated Breast: Fig. 9 shows reconstructed results from the 935 ml breast-only measurements, where both lesions are located in the same transaxial plane. Without additional torso contamination, and with a uniform breast background, both the centrally located 8 mm and the proximally located 5 mm diameter lesions are clearly visible. Table IV gives results from calculations of SNR and contrast for both lesions at the 2nd OSEM iteration (which was the optimal trade-off between gains in contrast and losses in SNR).

2) Breast with Filled Torso: Fig. 10(a) shows reconstructed results from the 1060 ml breast and filled anthropomorphic torso phantom measurements, for the centrally located 9.5 mm diameter lesion. Fig. 10(b) shows an example of reconstructed results for the 8 mm lesion. Table IV lists results from calculations of SNR and contrast for both the 9.5 mm and 8 mm lesions at the 2nd OSEM iteration.

C. Discussion

In studies with only the 935 ml breast filled, high-count, low-noise images result (Fig. 9). This is not surprising given the fairly large energy window (±8%) and large absolute activity. However, this ideal case does demonstrate the ability of the system to clearly resolve a 5 mm lesion. Furthermore, both sub-centimeter diameter lesions were resolved with each more-nearly-complete 3D sampling scheme afforded by the flexibility of the hemispherical positioning gantry, suggesting the viability of these trajectories for clinical studies. With the use of a radio-opaque bed to shield the system from background, we may expect the image quality, given enough statistics, to resemble that shown in these isolated breast measurements.

The TPB orbit (which does not strictly meet Orlov's sufficiency condition) yields the lowest SNR value for the 5 mm lesion and images, which are riddled with artifacts, including an elongated nipple-chest axis, similar to results seen in [8], [9]. With the more-nearly-completely sampled orbits, the breast shape is almost fully recovered. Results also indicate that the orbit most optimal for various lesion locations may change: for the 8 mm lesion, CP2A provides the highest SNRs, while for the 5 mm lesion, Cloverleaf provides the highest SNRs. Whether this result is more ascribable to the placement of the lesion or the size of the lesion itself is being further investigated.

The viewable breast volume is limited for the 935 ml breast case along the nipple-chest axis. Because the design criteria included meeting Orlov's criteria, the COR was located at the nipple for this particular breast shape and size. Thus, with the lesions optimally placed near the nipple for this set of measurements, resulting images provided for high contrast resolution. For lesions located near the chest wall, however, a COR located at the nipple may preclude their visualization given more-nearly-complete sampling. Consequently, design criteria for any orbit require a trade-off between more-nearly-complete sampling and viewable breast volume. This subsequent optimization of orbit design parameters was examined in the 1060 ml breast + filled torso experiments. The design goal for the orbit implementations for those measurements was to move the COR as far into the breast as practicable. Accordingly, the minimum tilt was increased from 0° to 15° so that the COR could be moved into the breast ~2 cm. This, in turn, increased the viewable breast volume. Indeed, the entire 12cm length of the nipple-chest wall axis can be seen, as well as some additional depth into the chest wall with only a small missing cone of data behind the chest wall along the nipple-chest axis.

With more realistic uptake ratios in the body and absolute activities of the organs, the 9.5 mm (0.43 ml) centrally-located lesion (~6 cm from the nipple) was discernible in all images. Again, results from the TPB orbit in Fig. 10 demonstrate the familiar elongation of the nipple-chest axis. Additionally, increased activity from the background, specifically the liver, is also visible (Fig. 10, white arrow). Interestingly, the remaining orbits, though also incompletely sampling the breast, appear to more nearly recover the breast's shape. This suggests that while the mathematical condition for accurate reconstruction of the activity distribution within the breast was not met, in practice, the sampling requirement may be less strict than initially anticipated; this is an area that warrants further investigation. Incomplete sampling may, however, produce false positives in the image (Fig. 10, CLOVER); this may also be due to other reconstruction artifacts since these misleading signals are actually manifested as streaks and appear in multiple contiguous planes. The more peripheral areas of the breast along the chest wall may suffer from less sufficient sampling; the uniformity of the sampling scheme itself is currently being investigated in addition to completeness issues.

For this work, there was no patient (torso) shielding whatsoever. Given a radio-opaque support bed, however, background activity should be significantly reduced, as the heart and liver should be removed from a significant number of detector vantages. Our group is in the process of implementing and investigating such a patient bed and its effects (and expected improvements) on image quality.

IV. CONCLUSIONS

The characteristics of a full FOV CZT detector were evaluated for dedicated SPECT imaging of the breast. The detector was found to have an 8% FWHM at 140 keV, and was able to clearly discern 3.1 mm diameter mini-rods. The key benefit provided by a dedicated, compact SPECT breast imaging system is its ability to acquire data about an *uncompressed*, pendant breast and potentially anterior chest wall. As a potential secondary diagnostic tool, the 3D sampling scheme can be tailored to an individual patient, especially if mammographic studies can provide *a priori* information about a suspected lesion. The phantom studies shown here demonstrate the capability of the system to easily adapt acquisition scheme for imaging of various breast shapes and sizes. Furthermore, results from phantom measurements reveal the ability of this approach to visualize tumors <1 cm in diameter. The strength of this molecular imaging approach for breast imaging can be further enhanced with additional structural information provided by transmission cone-beam mammotomography. Initial studies to develop a quasi-monochromatic beam and prototype computed mammotomograph for such a purpose are being undertaken by McKinley, et al. [30]. The 3D mammotomography system evaluated within this work, incorporating a compact CZT detector, shows a promising technique for imaging of the breast using clinically relevant scan times.

V. ACKNOWLEDGMENTS

The authors thank K. Parnham, J. Li, and B.E. Patt (*Gamma Medica*) for their assistance with camera operation and modification. MPT is a scientific advisor to *Gamma Medica*.

REFERENCES

[1] J. R. Buscombe, J. B. Cwikla, B. Holloway, and A. J. W. Hilson, "Prediction of the usefulness of combined mammography and scintimammography in suspected breast cancer using ROC curves," *J. Nucl. Med.*, vol. 42, pp. 3-8, 2001.

[2] I. Khalkhali, J. K. Baum, J. Villanueva-Meyer, S. L. Edell, L. G. Hanelin, C. E. Lugo, R. Taillefer, L. M. Freeman, C. E. Neal, A. M. Scheff, J. L. Connolly, S. J. Schnitt, M. J. Houlihan, J. S. Sampalis, and S. B. Haber, "99mTc sestamibi breast imaging for the examination of patients with dense and fatty breasts: multicenter study," *Radiology*, vol. 222, pp. 149-155, 2002.

[3] L. R. Coover, G. Caravaglia, and P. Kuhn, "Scintimammography with dedicated breast camera detects and localizes occult carcinoma," *J. Nucl. Med.*, vol. 45, pp. 553-558, 2004.

[4] M. B. Williams, A. R. Goode, V. Galbis-Reig, S. Majewski, A. G. Weisenberger, and R. Wojcik, "Performance of a PSPMT based detector for scintimammography," *Phys. Med. Biol.*, vol. 45, pp. 781-800, 2000.

[5] S. Majewski, D. Kieper, E. Curran, C. Keppel, B. Kross, A. Palumbo, V. Popov, A. G. Weisenberger, B. Welch, R. Wojcik, M. B. Williams, A. R. Goode, M. More, and G. Zhang, "Optimization of dedicated scintimammography procedure using detector prototypes and compressible phantoms," *IEEE Trans. Nucl. Sci.*, vol. 48, no. 3, pp. 822-829, 2001.

[6] J. Kim, Y. Choi, K. Joo, B. Sihn, J. Chong, S. E. Kim, K. H. Lee, Y. S. Choe, and B. Kim, "Development of a miniature scintillation camera using an NaI(Tl) scintillator and PSPMT for scintimammography," *Phys. Med. Biol.*, vol. 45, pp. 3481-3488, 2000.

[7] D. P. McElroy, E. J. Hoffman, L. MacDonald, B. E. Patt, J. S. Iwanczyk, Y. Yamaguchi, and C. S. Levin, "Evaluation of breast tumor detectability with two dedicated, compact scintillation cameras," *IEEE Trans. Nucl. Sci.*, vol. 49, pp. 794-802, 2002.

[8] M. P. Tornai, J. E. Bowsher, C. N. Archer, J. Peter, R. J. Jaszczak, L. R. MacDonald, B. E. Patt, and J. S. Iwanczyk, "A 3D gantry single photon emission tomograph with hemispherical coverage for dedicated breast imaging," *Nucl. Inst. Meth.*, vol. A497, no. 1, pp. 157-167, 2003.

[9] C. N. Archer, M. P. Tornai, J. E. Bowsher, S. D. Metzler, B. C. Pieper, and R. J. Jaszczak, "Implementation and initial characterization of acquisition orbits with a dedicated emission mammotomograph," *IEEE Trans. Nucl. Sci.*, vol. 50, no. 3, pp. 418-420, 2003.

[10] M. Singh and E. Mumcuoglu, "Design of a CZT based BreastSPECT system," *IEEE Trans. Nucl. Sci.*, vol. 45, no. 3, pp. 1158-1165, 1998.

[11] B. Mueller, M. K. OConner, I. Blevis, D. J. Rhodes, R. Smith, D. A. Collins, and S. W Phillips, "Evaluation of a small cadmium zinc telluride detector for scintimammography," *J. Nucl. Med.*, vol. 44, pp. 602-609, 2003.

[12] H. Wang, C. Scarfone, K. L. Greer, R. E. Coleman, and R. J. Jaszczak, "Prone breast tumor imaging using vertical axis-of-rotation (VAOR) SPECT systems: an initial study," *IEEE Trans. Nucl. Sci.*, vol. 44, pp. 1271-1276, 1997.

[13] B. C. Pieper, J. E. Bowsher, M. P. Tornai, J. Peter, and R. J. Jaszczak, "Breast tumor imaging using tiltable head SPECT cameras," *IEEE Trans. Nucl. Sci.*, vol. 48, no. 4, pp. 1477-1492, 2001.

[14] S. D. Metzler, J. E. Bowsher, M. P. Tornai, B. C. Pieper, J. Peter, and R. J. Jaszczak, "SPECT breast imaging combining horizontal and vertical axes of rotation," *IEEE Trans. Nucl. Sci.*, vol. 49, no. 1, pp. 31-36, 2002.

[15] M. P. Tornai, C. N. Archer, J. E. Bowsher, B. E. Patt, J. S. Iwanczyk, L. R. MacDonald, K. Parnham, "Feasibility of full-field single photon emission mammotomography using a novel CZT detector," *IEEE Nucl. Sci. Symposium Conf. Rec.*, vol. 3, pp. 1901, 2002.

[16] R. Pani, A. Soluri, R. Scafe, R. Pellegrini, G. de Vincentis, M. N. Cinti, M. Betti, R. Inches, G. Garibaldi, F. Cusanno, M. Gambaccini, A. Fantini, A. Taibi, A. Olivo, S. Pani, L. Rigon, D. Bollini, N. Lanconelli, and A. Del Guerra, "Feasibility study for SPECT mammography based on compact imagers rotating around breast vertical axis," *IEEE Nucl. Sci. Symposium Conf. Rec.*, vol. 3, pp. 21/36-21/39, 2000.

[17] M. P. Tornai, J. E. Bowsher, R. J. Jaszczak, B. C. Pieper, K. L. Greer, P. H. Hardenbergh, and R. E. Coleman, "Mammotomography with pinhole incomplete circular orbit SPECT," *J. Nucl. Med.*, vol. 44, pp. 585-593, 2003.

[18] J. E. Bowsher, M. P. Tornai, S. D. Metzler, J. Peter, and R. J. Jaszczak, "SPECT breast imaging using more nearly complete orbits and combined pinhole-parallel-beam collimation," *IEEE Nucl. Sci. Symposium Conf. Rec.*, vol. 3, pp. 1328-1330, 2001.

[19] NEMA Standards Publication NU 1-2001, "Performance measurements of scintillation cameras."

[20] H.M. Hudson and R.S. Larkin, "Accelerated image reconstruction using ordered subsets of projection data," *IEEE Trans. Medical Imaging*, vol. 13, no. 4, pp. 601-609, 1994.

[21] J. E. Bowsher, D. R. Gilland, C. E. Floyd, R. J. Jaszczak, V. E. Johnson, and R. E. Coleman, "Three dimensional iterative reconstruction for SPECT," *J. Nucl. Med.*, vol. 33, p. 879, 1992 (abstract).

[22] S. S. Orlov, "Theory of three dimensional reconstruction," *Sov. Phys. Crystallogr.*, vol. 20, no. 3, pp. 312-314, 1975.

[23] S. D. Metzler, J. E. Bowsher, and R. J. Jaszczak, "Geometrical similarities of the Orlov and Tuy sampling criteria and a numerical algorithm for assessing sampling completeness," *IEEE Trans. Nucl. Sci.*, vol. 50, no. 5, pp. 1550-1555, 2003.

[24] H. K. Tuy, "An inversion formula for cone-beam reconstruction," *SIAM J. Appl. Math.*, vol. 43, pp. 546-552, 1983.

[25] F. Scopinaro, R. Pani, G. De Vincentis, A. Soluri, R. Pellegrini, and L. Porfiri, "High-resolution scintimammography improves the accuracy of technetium-99m methoxyisobutylisonitrile scintimammography: use of a new dedicated gamma camera," *Eur. J. Nucl. Med.*, vol. 26, pp. 1279-1288, 1999.

[26] J. Maublant, M. de Latour, D. Mestas, A. Clemenson, S. Charrier, V. Feillel, G. Le Bouedec, P. Kaufmann, J. Dauplat and A. Veyre, "Technetium-99m-sestamibi uptake in breast tumor and associated lymph nodes, " *J. Nucl. Med.*, vol. 37, no. 6, pp. 922-925, 1996.

[27] R. Pani, G. De Vincentis, F. Scopinaro, R. Pellegrini, A. Soluri, I.N. Weinberg, A. Pergola, R. Scafe, and G. Trotta, "Dedicated gamma camera for single photon emission mammography (SPEM)," *IEEE Trans. Nucl. Sci.*, vol. 45, no. 6, pp. 3127-3133, 1998.

[28] M. B. Williams, D. Narayanan, M. J. More, P. J. Goodale, S. Majewski, and D. A. Kieper, "Analysis of position-dependent compton scatter in scintimammography with mild compression," *IEEE Trans. Nucl. Sci.*, vol. 50, no. 5, pp. 1643-1649, 2003.

[29] F. J. Th. Wackers, D. S. Berman, J. Maddahi, D. D. Watson, G. A. Beller, H. W. Strauss, C. A. Boucher, M. Picard, B. L. Holman, R. Fridrich, E. Inglese, B. Delaloye, A. Bischof-Delaloye, L. Camin, and K. McKusick, "Technetium-99m hexakis 2-methoxyisobutyl isonitrile: human biodistribution, dosimetry, safety, and preliminary comparison to thallium-201 for myocardial perfusion imaging," *J. Nucl. Med.*, vol. 30, no. 3, pp. 301-311, 1989.

[30] R.L. McKinley, M.P. Tornai, E. Samei, and M.L. Bradshaw, "Simulation study of a quasi-monochromatic beam for x-ray computed mammotomography," *Med. Phys.*, vol. 31, no. 4, pp. 800-813, 2004.

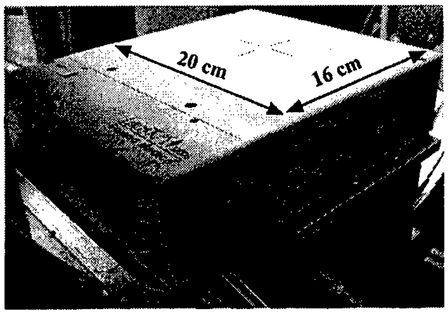

Fig. 1. Photograph of the compact CZT detector, the LumaGEM^{TM} 3200-S, with 16 x 20 cm^2 FOV.

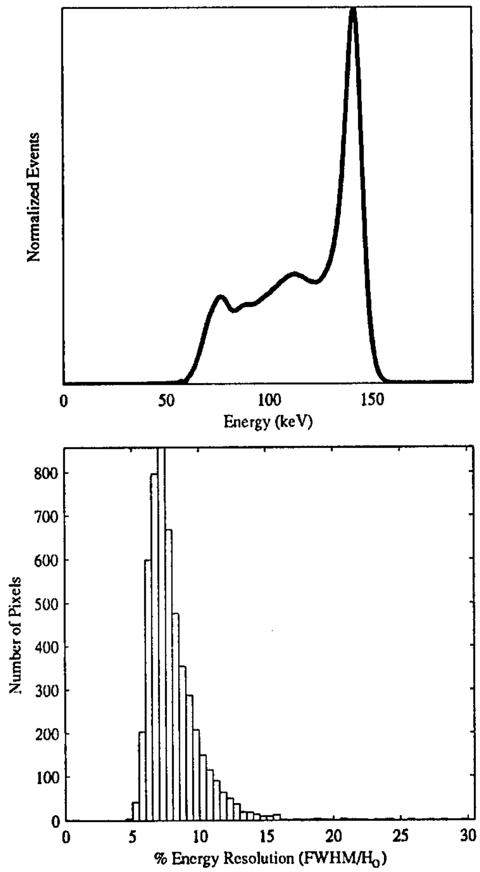

Fig. 2. (Top) Gain balanced, summed energy spectra of all active pixels. As per NEMA-2001 specifications, the measured energy resolution was 8.0%. (Bottom) Histogram of Energy Resolution for all discrete pixels. Mean = 8.0%; Median = 7.5%; Min = 4.8%; Max = 33.1%.

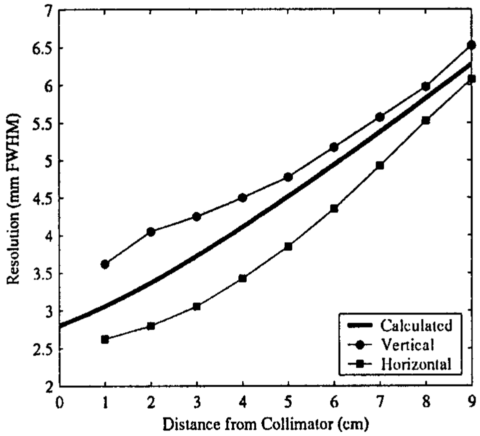

Fig. 3. Planar Spatial Resolution. Results from capillary line source measurements match calculated values. Horizontal and vertical measurements are slightly different, which may be due to the line source being ideally aligned with the collimator holes in one case, and/or non-alignment with the Cartesian distribution of the quantized pixels.

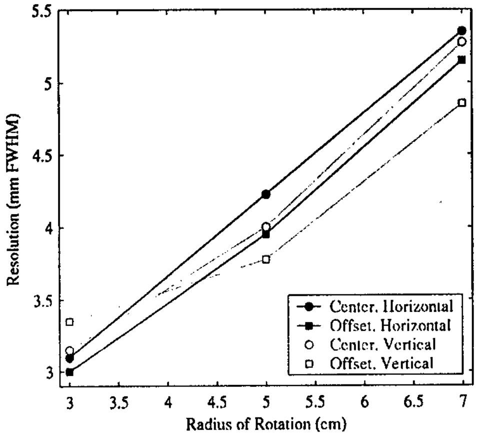

Fig. 4. Reconstructed SPECT spatial resolution. Results measured through two capillary tubes located at the ROR center and 2 cm offset. Data obtained from profiles drawn in both the horizontal and vertical directions from fifth iteration reconstructed data with fifteen summed slices.

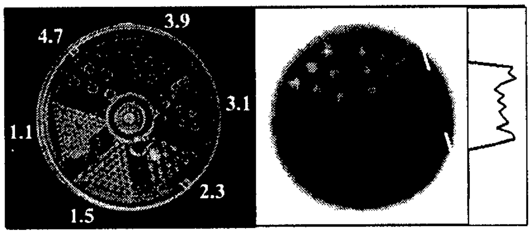

Fig. 5. (Left) Photograph of the mini-rod phantom, with diameters labeled (in mm), with a pitch equal to twice their diameter. (Middle) OSEM reconstructed mini-rod data (8 subsets, 20 iterations, 2.5 mm voxels, 5 summed slices to reduce noise, correction for COR partial pixel shift) acquired with 4.4 cm ROR. (Right) Profile drawn through the 3.1 mm rods at edge, as indicated.

Fig. 6. Dedicated Emission Mammotomography system with LumaGEM^{TM} 3200-S mounted on the hemispherical gantry. A filled anthropomorphic torso phantom and pendant, uncompressed 1060 ml breast are suspended within the camera's FOV.

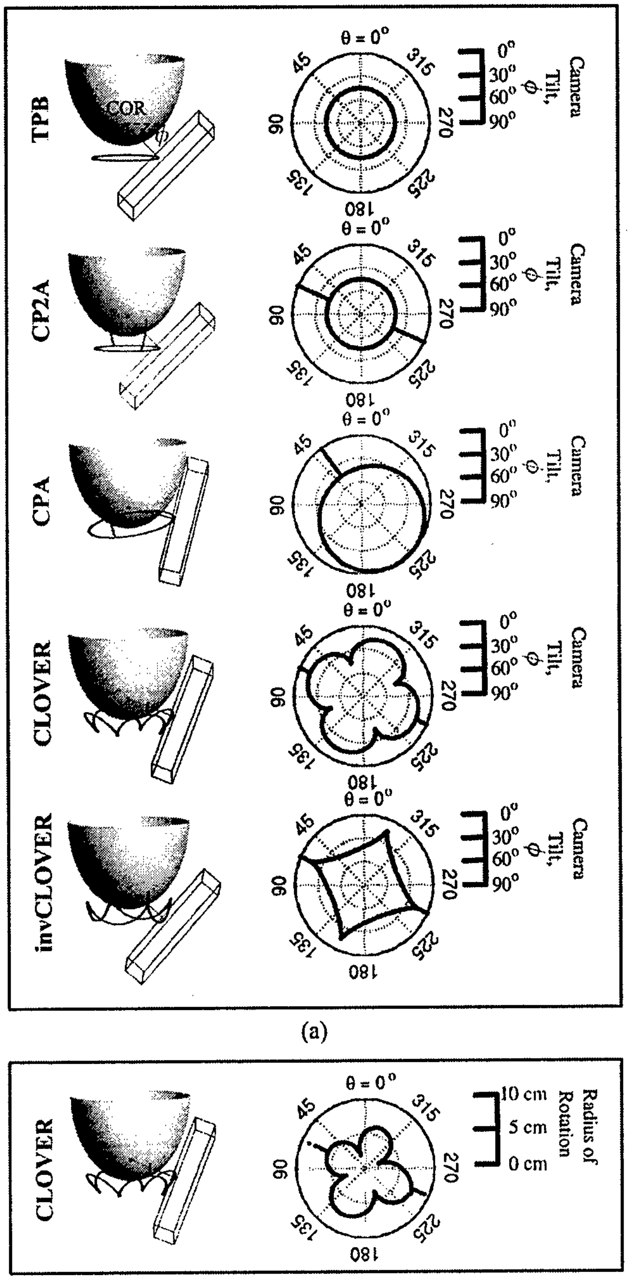

(a)

(b)

Fig. 7. (a) Scale schematics of orbits, with 1060 ml breast modeled. The wire-frame box represents the 16 x 20 cm^2 active detector FOV, with center on the trajectory (black orbit path) about the breast. Orbits are (Top to Bottom): Tilted-Parallel-Beam (TPB); Circle-Plus-Two-Arcs (CP2A); Circle-Plus-Arc (CPA); Cloverleaf (CLOVER); and Inverse Cloverleaf (invCLOVER) (see also Table I). Labeled in TPB schematic are the: (1) center of rotation (COR), located ~2 cm inside the breast along the nipple-chest axis; (2) direction of increased polar camera tilt (small arrow). Dark gray line from COR is perpendicular to the detector face. Note that while these implementations meet Orlov's criteria for sufficient sampling, simple modifications allow for more viewable breast volume when physical hindrances preclude sufficient sampling. Next to each 3D schematic are polar plots of camera polar tilt (ϕ) (plotted as a radius, with 90° at center and 0° at edge) versus azimuthal angle (θ) (plotted around the circle from 0° to 360°). (b) For Clover orbit, example polar plot of ROR contouring (radius from center), which allows camera to move close to the breast, as a function of azimuthal angle (θ).

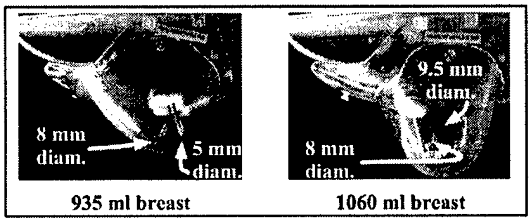

Fig. 8. Photographs of the 935 ml (left) and 1060 ml (right) anthropomorphic breast phantoms. Dimensions of both phantoms are given in Table II. Two sets of embedded lesions were inserted into each phantom as shown.

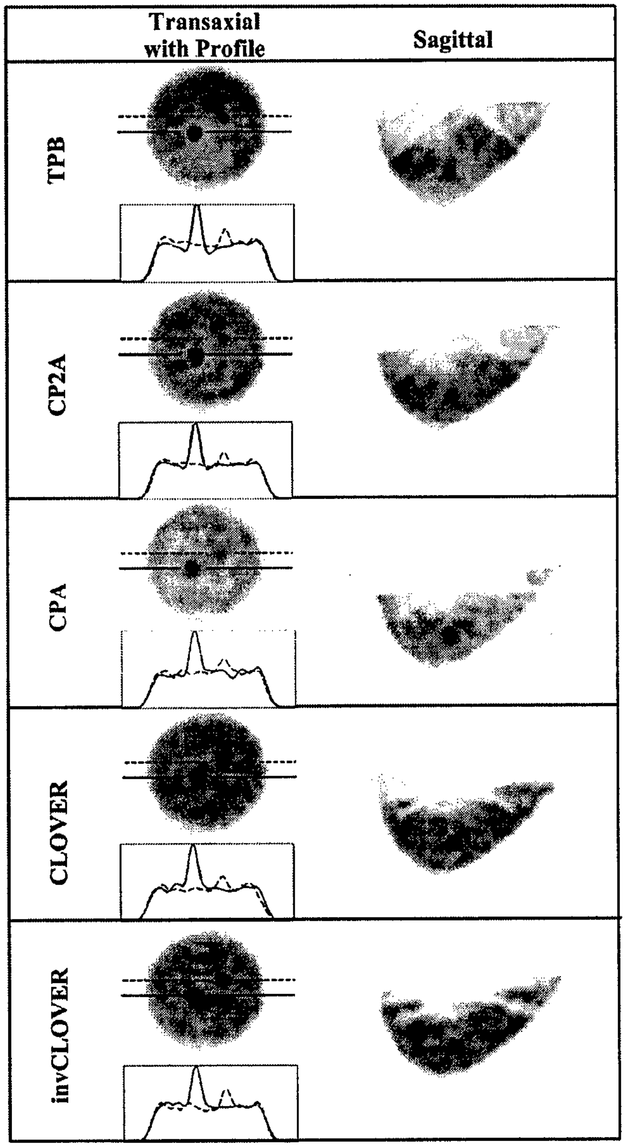

Fig. 9. OSEM reconstructed data (8 subsets, 2nd iteration shown) from the 935 ml breast data, for each labeled orbit, with a 9.8:1 lesion:breast radionuclide concentration ratio. Solid line in transaxial slice and profile is through the 8 mm lesion, and the dashed line is through the 5 mm lesion. Note that incomplete sampling artifacts from reconstructed data seen with the TPB orbit sagittal views are reduced with the more-nearly completely sampled orbits, similar to results shown in [8], [9].

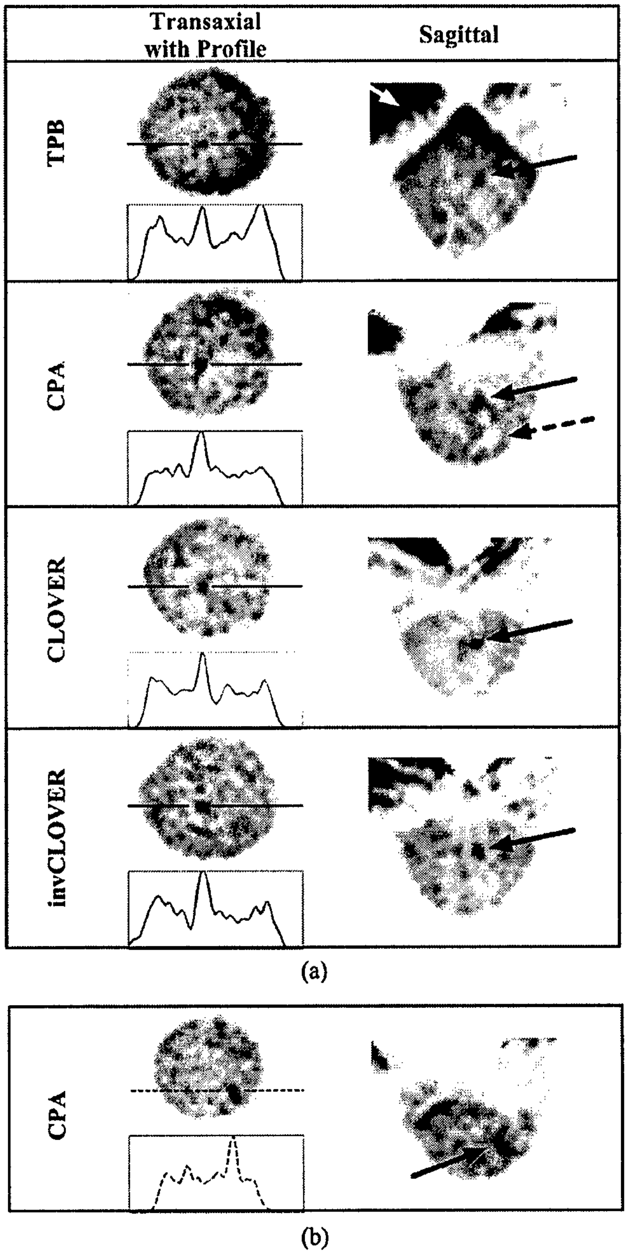

Fig. 10. OSEM reconstructed data (8 subsets, 2nd iteration shown) from the 1060 ml breast + filled torso data, for each labeled orbit with an incomplete sampling scheme, with a 6.1:1:12 lesion:breast-and-torso:liver-and-heart radionuclide concentration ratio. (a) Solid line is drawn through the 9.5 mm lesion. Note the increased background contamination with TPB (white arrow) as compared to the other orbits which do not maintain the large detector polar tilts, thus limiting more direct views of the heart and liver. Even with these less-completely sampled orbits, and more realistic absolute radioactivities within the phantom, the centrally located 9.5 mm lesion is clearly visible. Dashed arrow in CPA points to cold lesion holder, which can also be seen with the other orbits (see also InvClover) and in Fig. 8. (b) Dashed line is through the 8 mm lesion at different transaxial and sagittal locations than the larger lesion.

APPENDIX E

Comparison of Compact Gamma Cameras with 1.3mm and 2.0mm Quantized Elements for Dedicated Emission Mammotomography

Martin P. Tornai, *Member, IEEE*, Caryl N. Brzymialkiewicz, *Member, IEEE*, Marques L. Bradshaw, *Member, IEEE*, James E. Bowsher, *Member, IEEE*, Bradley E. Patt, *Member, IEEE*, Jan S. Iwanczyk, *Senior Member, IEEE*, Joshua Li, *Member, IEEE*, and Lawrence R. MacDonald, *Member, IEEE*

Abstract-- In an effort to image smaller breast lesions, two compact gamma cameras with different intrinsic NaI(Tl) pixel sizes are evaluated for use in the Application Specific Emission Tomography system for dedicated mammotomographic emission imaging. Comparison measurements were made with two scintillator arrays having 1.3x1.3x6mm^3 or 2.0x2.0x6mm^3 elements on exactly the same set of PMTs, electronics and control/processing hardware. Uniformity, sensitivity and energy resolution were assessed with flood field phantoms. Spatial resolution measurements included: a ^{99m}Tc (140keV) activity filled capillary tube imaged in planar mode from 1 - 10cm distance; two such tubes separated by 2cm were also imaged with simple circular tomography from 3 - 7cm radii-of-rotation (RORs); and a ^{99m}Tc filled mini-cold rod phantom was imaged at 5cm ROR with a simple circular orbit. Finally, a freely suspended and uniformly filled 950ml breast phantom containing four fillable lesions (4 - 10mm dia) was imaged with a lesion-to-uniform-background activity concentration ratio of 15:1, using simple and complex 3D orbits and minimal RORs. The measured sensitivity varied by the crystal fill-factor; uniformity had <4% variability; and mean energy resolutions of each camera were ≤12% full-width at half-maximum (FWHM). The planar spatial resolutions correspond to calculated values, with smaller pixels yielding 2 - 13% better resolution with decreasing separation distance; tomographic results ranged from 3.2 - 5.2mm FWHM at 3 - 7cm, with nominally better contrast-resolution for the smaller pixel camera. Consistent with signal detection characteristics for these measurement conditions, quantitative SNRs and contrasts from lesion imaging with the uniform breast background illustrate better overall performance under nearly all conditions and for all lesions for the larger pixel camera.

Introduction

WE are actively developing and integrating a dedicated Application Specific Emission Tomograph (ASET) system for mammotomographic emission imaging with single photon emission computed tomography (SPECT) [1-3]. Compact and dedicated cameras facilitate close proximity imaging, and can be implemented on novel geometries to acquire arbitrary trajectories about a pendant breast on an inverted hemispherical space. Further, the use of single photon detection versus coincidence detection for full tomography precludes the use of a necessary back-side detector which can physically interfere with lines of sight through the breast, and also limit the measurable breast and anterior chest volumes. By facilitating close proximity imaging relative to contemporary clinical gamma cameras, the ASET gantry thus permits higher sensitivity collimators to be used without substantially degrading spatial resolution.

Moreover, in an effort to image smaller breast lesions, two compact gamma cameras with different intrinsic NaI(Tl) pixel sizes are evaluated for use on the ASET. The exact same photomultipliers (PMTs), electronics, and additional control/processing hardware and software were used to compare identical imaging paradigms with each system. This way, the intrinsic differences of the quantized scintillator arrays could be quantitatively evaluated. The main caveat in this imaging evaluation is the assumption of a uniformly distributed breast background relative to the hot lesions [4]; clinically, it is well recognized that uptake and distribution of ^{99m}Tc labeled compounds is somewhat non-uniform in the breast [5-7]. Nevertheless, intrinsic characteristics of the camera systems can be compared, as well as their general phantom imaging performance.

Materials & Methods

Gamma Cameras

The *LumaGEM*™ model gamma cameras were developed by and obtained from *Gamma Medica, Inc.* (Northridge, CA) for a variety of imaging purposes, and are used here in the ASET [1-3]. The camera back-ends consist of small, square metal channel dynode position sensitive PMTs read-out through charge division networks and additional custom electronics boards, with modified control and data management software [8,9].

Two sizes of front-end scintillator arrays were investigated. The first consisted of 1.3x1.3x6.0mm^3 NaI(Tl) elements on 1.5mm pitch, in a 84x84 element array; this array had an ~84% fill factor. The second consisted of 2.0x2.0x6.0mm^3 NaI(Tl) elements on 2.2mm pitch, in a 58x58 element array; this array had an ~94% fill factor. The arrays were commercially obtained from the same manufacturer (*Bicron/St. Gobain*, Newbury, OH) to attempt to ensure that the manufacturing and processing, including use of inter-element reflective epoxy, was process independent.

The collimator used was a parallel beam, lead, hexagonal hole type with 25.4mm height, 1.22mm flat-to-flat hole size, and 0.2mm septa.

Phantoms & Acquisition

The flood field uniformity was measured with a 1cm thick phantom filled with aqueous ^{99m}Tc and which covered the entire camera field-of-view (FOV). The energy resolution was obtained for each usable pixel from the list mode collected flood data. A similarly thick, but smaller rectangular phantom was used to evaluate the overall system sensitivity at 10cm separation distance according to the NEMA specifications [10].

Planar and SPECT measurements were made for each system to determine the full-width at half-maximum (FWHM) line spread functions (LSFs). A single 0.9mm inner-diameter glass capillary tube was used in air for the planar measurements. First, the line source and camera were leveled, and the line was horizontally oriented relative to the camera face; then, 1cm from the collimator face, the line source was stepped in 0.1mm increments for a total distance just longer than each respective camera's pixel pitch in the orthogonal direction of line orientation, and images acquired for short durations with a -5%+10% wide asymmetric energy window about 140keV. From the acquired images, the FWHMs were obtained, and the line source was repositioned to the location of the minimum FWHM in order to center it over a row of pixels. Multiple measurements were then made at distances from 1-10cm from the collimator face by backing the camera away from the line source. The camera was then rotated 90° on the ASET gantry, and the LSF measurements were repeated in the vertical orientation without pixel-row centering. Prior to FWHM determination, 14 and 12 rows of pixels, for the 1.3mm and 2.0mm pixel systems respectively, were summed to further reduce image noise, but this may also have contributed to a larger measured LSF if the capillary tube was not perfectly oriented along the Cartesian detector pixel distribution.

For the SPECT LSF measurements, two such vertically oriented capillary tubes were positioned 2cm from each other, with one tube nearly on the center of the axis of rotation. Each camera was set-up at 3 different radii-of-rotation (RORs) (3, 5, 7cm), and full 360° acquisitions with 128 projections were obtained and reconstructed with voxel driven ordered subsets expectation maximization (OSEM) using 8 subsets. Prior to FWHM determination in the horizontal and vertical reconstructed dimensions, 17 and 11 planes, respectively, were summed to further reduce image noise; as for the planar measurements, slice summing may have contributed to a larger measured width if the tube was not perfectly oriented along the Cartesian detector pixel distribution and/or if there was an angular offset (pitch or yaw) to the detector during the SPECT scans.

Further, an acrylic mini-cold rod phantom (model ECT/DLX-MP, *Data Spectrum Corp.*, Hillsborough, NC) was placed in a cylinder, with aqueous ^{99m}Tc and imaged for 1hour over 360° with 256 projection angles at a 5cm ROR. The rod sizes are 1.1, 1.5, 2.3, 3.1, 3.9, and 4.7mm Ø, and are arranged in 6 sectors. These frequency/resolution elements are spaced on twice their diameter in a hexagonal close packed distribution.

To simulate a clinical imaging paradigm, a freely suspended 950ml anthropomorphic breast phantom, along with breast lesions (models ECT/HOL-468/A, *Data Spectrum Corp.*) were also used in these measurements. The fillable lesions were approximately 4, 6, 8, and 10mm Ø. These phantoms were filled with aqueous ^{99m}Tc radioactivity in 15:1 ratio of lesion to uniform breast background activity concentrations. To reduce acquisition times to ~5min, the initial lesion concentration was increased to ~13.3μCi/ml during measurements with each camera system; these imaging times approximately correspond to 20min equivalent times for more realistic activity concentrations (i.e. much lower concentrations of ~3.3 μCi/ml). The tomographic acquisitions used the previously described shifted camera technique to image the large breast without truncation [2,3]. Two classes of orbital trajectories were investigated, as described in detail in [3,11]: nearly complete and incomplete sampling orbital trajectories. Of these classes, the complete or nearly complete sampling orbits include: tilted parallel beam (TPB) with 0° tilt, which is equivalent to a vertical axis of rotation (VAOR) orbit; circle plus 2 arcs (CP2A) which consists of a TPB orbit with polar tilt >0°, and two conjugate projection sampling arcs subtending the polar tilt range back to the horizon; and circle plus 4 arcs (CP4A) which consists of a CP2A-type orbit with two additional polar arcs azimuthally located 90° away from the arcs in CP2A. The incomplete sampling orbits include TPB orbits with polar tilt angle >0° but without any corresponding arcs returning the camera to the horizon. The range of investigated polar arcs (camera tilt) was from 0° to 45°, in 15° increments between measurements. A previously described voxel driven OSEM algorithm incorporating the Euler angles describing the camera trajectories [2,3,12] was used to reconstruct the acquired data.

TABLE 1.
INTRINSIC AND EXTRINSIC CAMERA CHARACTERISTICS

Characteristics	1.3mm Pixel Camera	2.0mm Pixel Camera
Usable Pixels (%)	94.2	89.2
Uniformity (%)	< ±4.3	< ±3.9
Sensitivity (cts/sec/MBq)	33.7	38.9
Mean Energy Resolution (%)	11.5	12.0
Max. Energy Resolution (%)	44.0	33.0
Min. Energy Resolution (%)	7.7	8.8

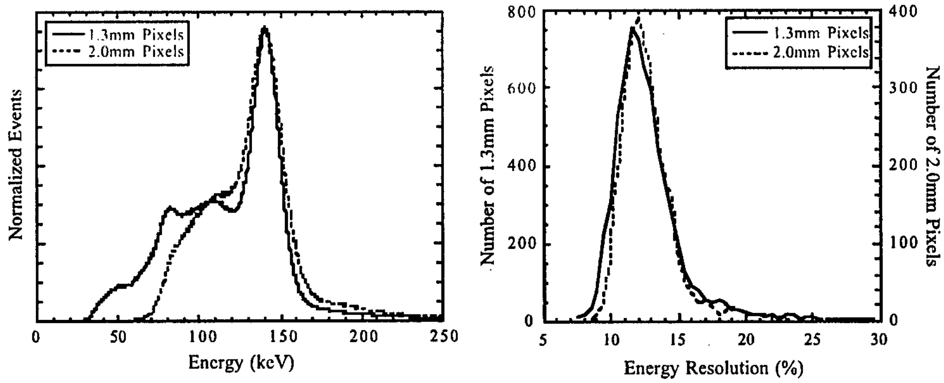

Fig. 1. (Left) Comparison of energy spectra, normalized to the photopeak maxima from ^{99m}Tc, obtained with flood fields from the 1.3mm and 2.0mm pixel cameras. Combined, gain balanced pixel photopeak widths from these spectra exhibit 15.2% and 19.9% FWHM, respectively. Different lower energy thresholds were used in the acquisitions. (Right) Histogram of the energy resolution distribution for each set of quantized pixels. Mean energy resolutions are 11.5% and 12.0% respectively, for the smaller and larger pixel cameras with the absolute ranges listed in Table 1.

Results & Discussion

Uniformity, Sensitivity and Energy Resolution

The overall intrinsic and extrinsic performance characteristics of each camera system were nearly identical (Table 1, Fig. 1). The <100% pixel utilization occurs due to difficulty of separating edge pixels in Anger-type, multiplexed charge division positioning maps with the pixel boundary drawing algorithms, partly occurring from optical coupling at the edges and partly from the charge division itself. It should be noted that in these imaging studies, the rows of unusable pixels predominantly occurred distal to the edge of each camera which can be brought into close proximity to the chest wall in scintimammographic applications.

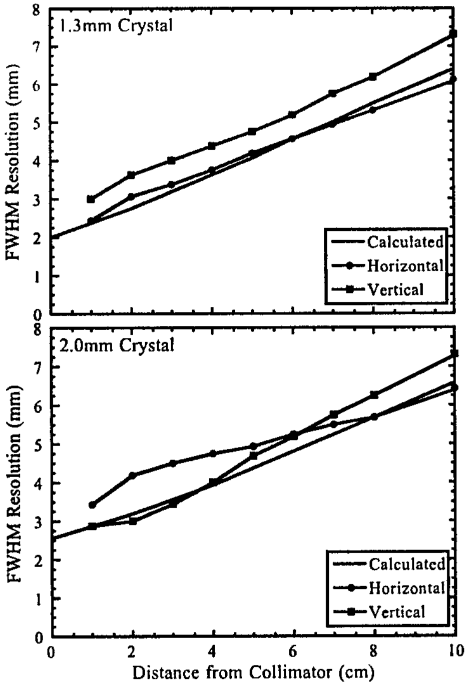

Fig. 2. Planar spatial resolution measured with the capillary line source compared with the calculated resolution for each camera. Differences in horizontal and vertical measurements may be due to alignment of the hexagonal close packed collimator hole arrangement with the Cartesian grid arrangement of the crystal arrays.

Overall, these results suggest some important findings: the difference in sensitivities can be accounted for by the fill factor difference; crystal array manufacturing is highly reproducible between arrays, even of different sized elements; smaller elements may indeed be utilized for higher resolution imaging purposes without substantial loss of performance; and intrinsic electronic signal processing limitations may play a more dominant role in camera performance, rather than limitations believed due to light extraction on crystal size alone [13].

Spatial Resolution Measurements

Not surprisingly, the planar LSF FWHMs corresponded to the values calculated from standard collimator equations, including intrinsic resolution, and were slightly better for the smaller pixel camera (Fig. 2). As appears true for single photon imaging pixellated cameras, the intrinsic resolution corresponds to the pixel size. Comparatively, the SPECT mean LSF FWHMs were nearly identical, with a greater spread in individual horizontal-vertical and center-offset measure-ments for the larger pixel camera (Fig. 3). A possible explanation for the larger variability of the resultant tomographic spatial resolution is that the line sources were not completely vertical between the acquisitions (or, as mentioned earlier, the camera was not completely vertically aligned), or indeed the line sources were between pixel row/columns in some projection views, thus having broader individual resolutions at some views relative to others and yielding broader, potentially non-circular reconstructed line sources in cross section. Due to the non-Gaussian detector response, in contrast to continuous crystal cameras, these rect response pixellated systems could yield broader resolution measures when the sources are located close to the camera face and between row/columns of pixels. Another possible explanation is simply due to aliasing of the 0.9mm line source with 2.2mm pixellation sampling.

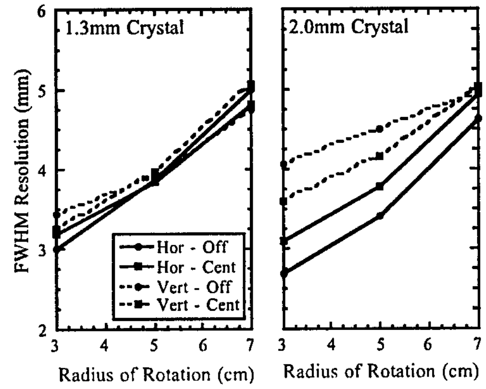

Fig. 3. SPECT spatial resolution measured in horizontal (Hor) and vertical (Vert) dimensions of the reconstructed images through the two capillary line sources located at the ROR center (Cent) and 2cm offset from center (Off). While there is overall smaller variation in resolution for any dimension or location as measured with the 1.3mm crystal camera, the means at a given ROR are similar.

While this work is intended to compare quantized element imaging systems, whose intrinsic spatial resolution is substantially better than continuous crystal systems and which can also provide energy spectra on a per pixel basis, an alternative comparison could be with a very high resolution continuous crystal camera. That is, by using a camera having a fixed sensitivity and intrinsic spatial resolution, the overall image resolution could be varied by changing the digitized pixel or image size. Indeed, it would seem likely that resolution aspects would follow the expected trends: larger digitized pixel size leads to poorer spatial resolution. The two important characteristics that pixellated systems have that continuous systems do not is that (1) the intrinsic resolution of the system is determined at the front-end, but physical pixel element size; (2) each pixel has its own associated, complete energy spectrum that can be evaluated, while continuous systems do not simply acquire this information. Thus, it is believed that there is are important differences between using these distinct crystal systems.

Tomographic reconstructions of the VAOR cold-rod data show somewhat better uniformity for the larger pixel camera with fewer artifacts, however, the smaller pixel camera yields qualitatively better contrast-resolution (Fig. 4). There was no spatial resolution nor attenuation correction modeled in the reconstructions, and voxel sizes correspond to the dimensions of the intrinsic pixellation of each camera system.

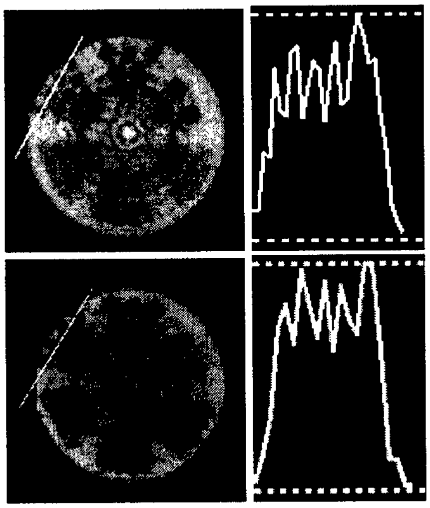

Fig. 4. OSEM reconstructed image data from 1hr, 256 angle, simple VAOR acquisitions at the exact same ROR of the mini-cold rod phantom from the (Top) 1.3mm crystal and (Bottom) 2.0mm crystal cameras. Rings are due to non-uniformity artifacts as is the "hot"/"cold" spot at center. Note slightly improved contrast resolution in associated profiles (single pixel width) at right through the 3.1mm Ø rods for smaller pixel camera. Image slices are summed as described.

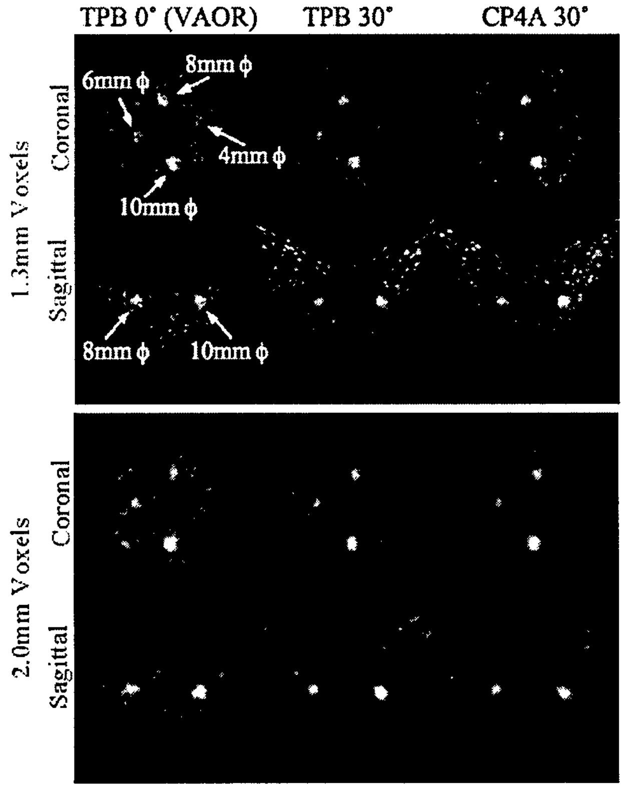

Fig. 5. OSEM reconstructed (2^{nd} iteration, 8 subsets) coronal and sagittal slices through various acquired data sets illustrating image quality and volumes of view of the freely suspended breast containing 4 lesions with 15:1 lesion to background ratios. Note increased viewable volume with tilted acquisitions

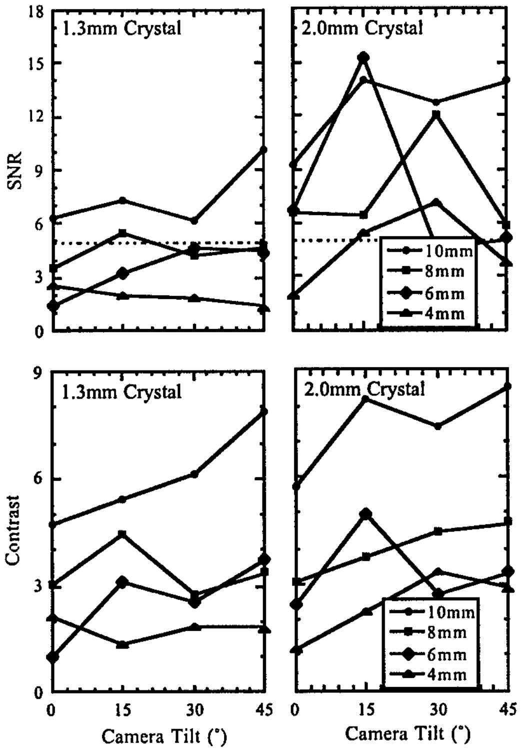

Fig. 6. SNR and Contrast values of TBP=0° calculated from ROIs about each of 4 known lesions and associated backgrounds with 15:1 activity concentration ratio, using simple (tilted) circular orbits about the suspended breast. Values were calculated from ROIs obtained from the 3^{rd} iteration. Dashed line in SNR plots indicates Rose's detectability threshold.

Breast Lesion Imaging Comparisons

A selection of the reconstructed images is shown in Fig. 5. Indeed, a large majority of the images were indistinguishable from one another, except for the reduced image volume of the sagittal sections of the TPB 0° scans. This reduced volume is one limitation of the simple VAOR imaging approach, another being the necessarily large ROR required to orbit the breast unhindered. In those images shown, while only the VAOR and CP4A orbits completely sample the breast volume, the images look qualitatively similar. This was somewhat unexpected, and the results are consistent [2,3,11]. Noise quality was smoother in the larger pixel images, and this is likely due to the larger voxel sizes. Stopping criteria with iterative reconstruction for noise versus bias estimates have been investigated for breast SPECT [12], but we utilized a stopping criteria trading-off signal-to-noise versus image contrast as in [2], and chose the 2nd OSEM iteration for display purposes and the 3rd OSEM iteration for SNR and contrast measurements. There was no post-reconstruction filtering, but this may improve image SNR further for both.

SNR was quantitatively measured as the difference in signal and background divided by the background noise; contrast was measured as the signal and background difference divided by the background. All values were obtained from lesion-sized regions of interest found by automatic 3D centroiding, described in detail in [11].

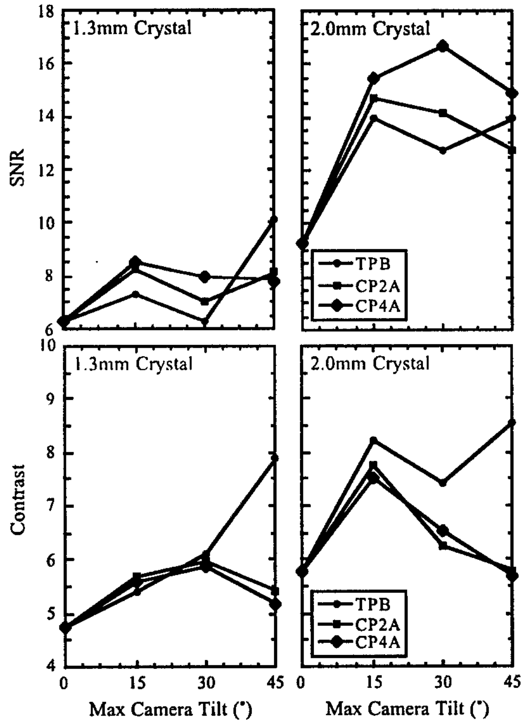

Fig. 7. SNR and contrast values calculated for ROIs about the 10mm lesion for each of the incompletely (TPB) and completely (CP*A) sampled breast volumes. Values were calculated from ROIs obtained from the 3rd iteration.

For the TPB-only data, which includes VAOR having the only completely sampled volume, the SNRs and contrasts for both cameras generally improve for all lesion sizes as the maximum tilt angle increases (Fig. 6); the majority of measured values involving a more complex orbit are better than for the TPB 0° case. Decreased ROR possible with camera tilt >0° may be one important factor that contributes to this result. The values obtained from larger lesions are higher overall, but this limitation may be due to the relatively few iterations used in the reconstruction. The larger lesions were more likely to have SNRs greater than Rose's threshold of detectability of SNR=5, indicating that *a priori* knowledge of the lesion locations in these measurements was helpful for the smaller lesions. Indeed, even the smallest lesion was ~4mm in diameter, which is larger than the intrinsic resolution of the larger pixel camera. Thus, the larger pixel camera would not alias the measured lesions, and, given better noise characteristics (better efficiency) thus yielded overall better SNR performance for the lesions.

With both cameras, the majority of measured SNRs and contrasts of the largest 10mm diameter lesion were better for all orbits than for the TPB 0° (VAOR) scan (Fig. 7). Similar to the incompletely sampled, TPB >0° orbits, these results may be in part due to the decreased ROR obtainable with these complex 3D orbits. While positive gains were realized for all orbits relative to VAOR, the larger pixel camera also outperformed the smaller pixel camera under these conditions.

The noticeably poorer SNR and contrast results of the smaller pixel camera in these lesion imaging paradigms may potentially be explained by the fact that the breast phantom background contained a uniform distribution of activity. That is, the lower frequencies due to the uniform background could be more easily measured by the camera system having a more sensitive lower frequency response [4] (i.e. the larger pixel camera); a random or otherwise non-uniform background may obviate these results in favor of the smaller, higher resolution imaging system. We are developing such a non-uniformly fillable breast phantom with which we could verify this conjecture. Furthermore, as was not the case here, it would be relevant to investigate imaging yet smaller objects whose size is smaller than the intrinsic resolution of the camera system, as it could be expected then that the system with better resolution response would yield superior SNR performance.

Conclusions

A quantized NaI(Tl) gamma camera with 1.3x1.3x6mm^3 elements has been developed and evaluated. It was also compared with an identical system having larger, 2x2x6mm^3 elements, and found to have similar energy, uniformity, and sensitivity performance. As could be expected, the planar and SPECT spatial resolutions measured for line sources in air were somewhat better for the smaller pixel camera, and this was additionally seen in the better contrast-resolution of tomographic measurements and OSEM reconstructions of a cold-rod frequency/resolution phantom. While it appears that the lesion imaging performance was slightly worse for the smaller pixel camera despite the nominally better intrinsic characteristics, this may be explained by measurement of the lesions on a uniform background, an object size that was larger than the intrinsic resolution of either system, and the better noise performance of the larger pixel camera; further investigations with non-uniform phantoms and smaller lesions are warranted to validate these conclusions. For now, pixels sizes on the order of 2 – 2.5mm appear to be well suited for emission mammotomography, and we are pursuing the use of a high-Z compound semiconductor, CZT [11], to replace similarly sized NaI(Tl) elements and exploit the superior energy resolution and detection efficiencies offered by that class of materials.

Acknowledgment

The authors would like to thank Dr. Craig Abbey for helpful discussions, Dr. Ronald Jaszczak for use of phantoms and lab space to perform these measurements, and the Duke Radiopharmacy for providing radioisotopes used in these studies. MPT is a scientific consultant to *Gamma Medica, Inc.*

References

[1] MP Tornai, JE Bowsher, CN Archer, *et al.* Dedicated breast imaging with an ASET: Application Specific Emission Tomograph. *J. Nucl. Med.* **42**(5):97P. 2001.

[2] MP Tornai, JE Bowsher, CN Archer, *et al.* A 3D gantry single photon emission tomograph with hemispherical coverage for dedicated breast imaging. *Nucl. Instr. Meth.* **A497**(1):157-167. 2003.

[3] CN Archer, MP Tornai, JE Bowsher, SD Metzler, BC Pieper, RJ Jaszczak. Implementation and initial characterization of acquisition orbits with a dedicated emission mammotomograph. *IEEE Trans. Nucl. Sci.* **NS-50**(3):413-420. 2003.

[4] JP Rolland, HH Barrett. Effect of random background inhomogeneity on observer detection performance. *J Opt Soc Am A.* **9**(5):649-58. 1992.

[5] RF Brem, JM Schoonjans, DA Kieper, *et al.* 2002. High-resolution scintimammography: a pilot study. *J. Nucl. Med.* **43**(7):909-915.

[6] E Itti, BE Patt, LE Diggles, *et al.* 2003. Improved scintimammography using a high-resolution camera mounted on an upright mammography gantry. *Nucl. Instr. Meth. Phys. Res.* **A497**(1):1-8.

[7] LR Coover, G Caravaglia, P Kuhn. 2004. Scintimammography with dedicated breast camera detects and localizes occult carcinoma. *J. Nucl. Med.* **45**(4):553-558.

[8] LR MacDonald, BE Patt, JS Iwanczyk, *et al.* LumaGEM: high-resolution dedicated gamma camera. *J Nucl Med.* **41**(5):56P. 2000.

[9] DP McElroy, EJ Hoffman, LR MacDonald, *et al.* Evaluation of performance of dedicated, compact scintillation cameras. *Proc. SPIE.* **4142**:231-241. 2000.

[10] Performance Measurements of Scintillation Cameras. *NEMA Standards Publication NU-2000.* Roslyn, VA.

[11] CN Archer, MP Tornai. Investigation of full-field CZT detector for emission mammotomography. *2003 IEEE Nuclear Science Symposium & Medical Imaging Conference Record* (CD-ROM ISBN 0-7803-8258-7).

[12] BC Pieper, JE Bowsher, MP Tornai, CN Archer, RJ Jaszczak. 2002. Parallel-beam tilted-head analytic SPECT reconstruction: derivation and comparison with OSEM. *IEEE Trans Nucl Sci.* **NS-49**(5):2394-2400.

[13]AJ Bird, T Carter, AJ Dean, D Ramsden, BW Swinyard. The optimisation of small CsI(Tl) gamma-ray detectors. *IEEE Trans Nucl Sci.* **NS-40**(4):395-399.